applied sciences

MDPI

Article

Petrogenesis of Early Cretaceous High Ba-Sr Granitoids in the Jiaodong Peninsula, East China: Insights into Regional Tectonic Transition

Zhongliang Wang [1,*], Rongxin Zhao [2], Tong Ye [3], Yu Wang [2], Mingchao Wu [1], Xuan Wang [4,5], Rifeng Zhang [6], Mingyun Li [1], Yabo Liu [1] and Jiahao Qiao [1]

[1] School of Earth Sciences and Resources, China University of Geosciences, Beijing 100083, China
[2] Jiaojia Gold Company, Shandong Gold Mining Stock Co., Ltd., Laizhou 261438, China
[3] Yunfu Natural Resources Bureau, Yunfu 527300, China
[4] MNR Key Laboratory of Metallogeny and Mineral Assesment, Institute of Mineral Resources, Chinese Academy of Geological Sciences, Beijing 100037, China
[5] School of Earth and Space Sciences, Peking University, Beijing 100871, China
[6] Yingkou Essential Industries High Quality Development Promotion Center, Yingkou 115003, China
* Correspondence: zlwang@cugb.edu.cn; Tel.: +86-10-82336549; Fax: +86-10-82322175

Abstract: Element geochemistry, Sr and Nd isotope, and LA-ICP-MS zircon U-Pb isotope data have been obtained for the granitoids of Dazesan pluton in the Jiaodong Peninsula, East China, and their intermediate microgranular dark enclaves so as to reveal their petrogenesis and tectonic implications. These granitoids have high SiO_2 (68.25–71.56 wt.%), K_2O (3.44–5.50 wt.%), total alkalis ($K_2O + Na_2O$ = 7.29–9.00 wt.%), Sr (451–638 ppm), Ba (1157–2842 ppm) and light rare earth elements (LREEs) (131.57–210.08), with strong depletion both in heavy rare earth element (HREE) and high field strength element (HFSE) concentrations as well as unclearly Eu anomalies, showing typical signatures of high Ba-Sr granitoids. They possess high $(La/Yb)_N$ (32–50) and Sr/Y (50–79) values and low MgO (0.76–1.11 wt.%), Cr (9.9–19.6 ppm) and Ni (4.51–7.04 ppm) concentrations. All the above geochemical compositions are similar to those of late Early Cretaceous granitoids, in combination with zircon LA-ICP-MS U-Pb ages of 119.6 ± 1.3 to 120 ± 1 Ma for these granitoids obtained in this study, indicating c. 120 Ma probably represents the lower limit of ages when late Early Cretaceous granitoids emplaced in the Jiaodong Peninsula. The microgranular dark enclaves, forming a linear trend with their host granitoids on the oxide against SiO_2 plots, display higher MgO contents of 3.05–4.39 wt.% at lower SiO_2 concentrations of 54.25–56.84 wt.% and possess a zircon LA-ICP-MS U-Pb age of 119 ± 2 Ma, identical to those of these granitoids, indicating the acid magma and intermediate magma were coeval. Furthermore, dark enclaves and their host granitoids have indistinguishable $(^{87}Sr/^{86}Sr)_i$ values of 0.709523–0.70972 and 0.709361–0.709858, respectively, and plot within a two-liquid immiscible field on the Greig pseudoternary phase diagram. In addition, they have markedly parallel REE patterns, with the dark enclaves having much greater REE and HFSE abundances than those of their host granitoids. Therefore, it is suggested that liquid immiscibility is a viable model to explain the chemical compositional variations between the Dazeshan granitoids and their dark enclaves. Based on the element geochemistry, geochronology and Sr- and Nd-isotope of the Dazeshan granitoids and their dark enclaves, it is envisaged the crust-derived acid melts due to partial melting of ancient continental lower crust in the Jiaodong Peninsula (mainly Neoarchean-Palaeoproterozoic basement in the Jiaobei terrane) containing a subduction-related material, resulting from the addition of the enriched subcontinental lithospheric mantle-derived melts, assimilated the lithospheric mantle-derived basic melts and formed the homogeneous magma chamber at the crust base, then split into two immiscible liquids, with one granitic liquid producing the Dazeshan granitoids and the other intermediate one forming the dark enclave during its ascent. Combined with previous studies, the identification of a lithospheric mantle-derived material in the Dazeshan granitoids suggests a catastrophic lithospheric thinning at c. 120 Ma, reflecting an abrupt change in the direction of Palaeo-Pacific plate subducting and the corresponding regional tectonic transition from E–W extension to NW–SE extension.

check for updates

Citation: Wang, Z.; Zhao, R.; Ye, T.; Wang, Y.; Wu, M.; Wang, X.; Zhang, R.; Li, M.; Liu, Y.; Qiao, J. Petrogenesis of Early Cretaceous High Ba-Sr Granitoids in the Jiaodong Peninsula, East China: Insights into Regional Tectonic Transition. *Appl. Sci.* **2023**, *13*, 1000. https://doi.org/10.3390/app13021000

Academic Editors: Andrea L. Rizzo and Dibyendu Sarkar

Received: 16 November 2022
Revised: 16 December 2022
Accepted: 23 December 2022
Published: 11 January 2023

Copyright: © 2023 by the authors. Licensee MDPI, Basel, Switzerland. This article is an open access article distributed under the terms and conditions of the Creative Commons Attribution (CC BY) license (https://creativecommons.org/licenses/by/4.0/).

Keywords: high Ba-Sr granitoids; dark enclaves; tectonic transition; MASH process; liquid immiscible; Jiaodong Peninsula

1. Introduction

East China, towards the west Pacific Ocean (Figure 1a), was transformed into an active continental margin due to Palaeo-Pacific plate subducting under East Asia at a shallow angle, which was initiated at c. 180 Ma [1–3], following the collision of the North China Craton (NCC) with the Yangtze Craton (YC) in the Middle-Late Triassic (244–220 Ma) [4]. The latter orogenesis resulted in the formation of the Jiaodong Peninsula, by the combination of Jiaobei terrane in the northwest with Sulu terrane in the southeast by way of the NE- to NNE-trending lithospheric-scale Wulian-Qingdao-Yantai Fault (WQYF), on the East China continental margin (Figure 1a,b) [5,6]. The Mesozoic tectonic evolution in the Jiaodong Peninsula was closely associated with the Palaeo-Pacific plate subduction [7,8], the varying velocity, angle, and direction of which caused the crustal deformations and changed the geodynamics of the overlying East China continental margin [8,9]. In particular, it has been suggested that a tectonic transition occurred in the Jiaodong Peninsula because of the changes in the direction of Palaeo-Pacific plate subducting during the late Early Cretaceous [8–11]. A shift of this period from extension to transpression, corresponding to a change from SW to NW in the direction of Palaeo-Pacific plate subducting during c. 125–122 Ma [8], has been inferred from the development of basins, extension-related igneous rocks and gold deposits in the Jiaodong Peninsula [8,10,11]. However, it was suggested that the stress regimes shifted from transpression to extension at c. 120 Ma, which was indicated by the sinistral to normal movement that the Tan-Lu Fault (TLF) experienced [12]. Furthermore, fault-slip data from the Jiaobei terrane showed an overall extensional tectonic regime during Early Cretaceous only with the extensional direction rotating from E–W to NW–SE at c. 120 Ma [13], corresponding to a change of the Palaeo-Pacific plate subduction direction from WNW (139–122 Ma) to NW (121–95 Ma) [14].

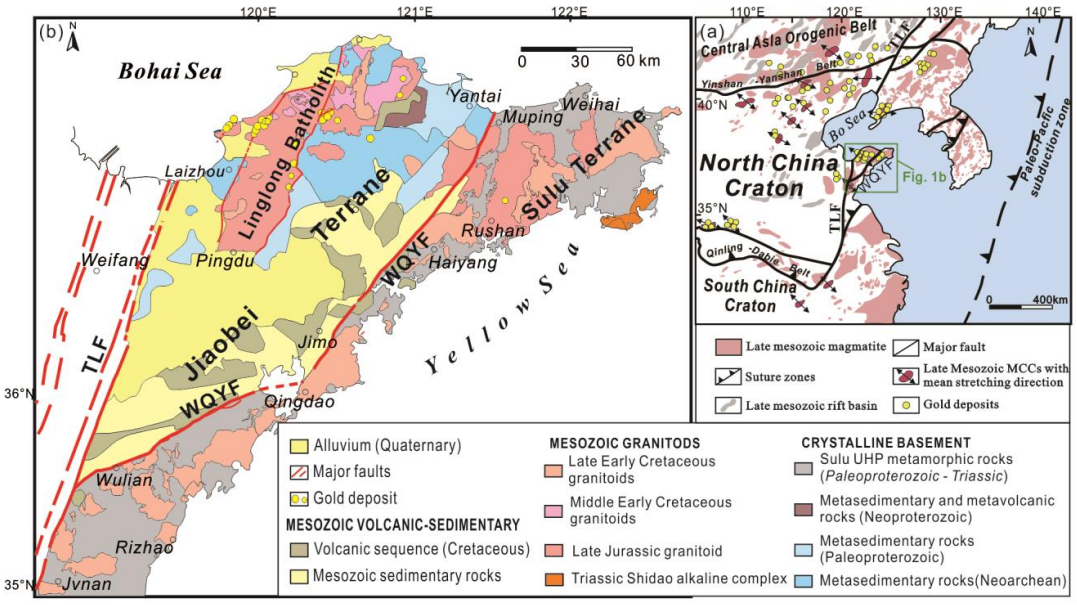


Figure 1. (**a**) Simplified tectonic map of East China illustrating the locations of Palaeo-Pacific subduction zone and Jiaodong Peninsula. Adapted with permission from [15]. (**b**) Simplified geological map of the Jiaodong Peninsula illustrating the major faults, large-scale Mesozoic magmatism, and typical gold deposits. Adapted with permission from [6]. Main faults: TLF, Tan-Lu Fault; WQYF, Wulian-Qingdao-Yantai Fault.

High Ba-Sr granitoids, occurring in Phanerozoic (especially Early Cretaceous and Tertiary) orogenic belts globally [16–18], were first defined by [16] based on their geochemical features, which are marked by high Ba (>500 ppm), Sr (>300 ppm), LREEs and K/Rb, as well as low Rb, U, Th, Ta, Y and HREEs, with strong Nb depletion and insignificant Eu anomaly [16,19,20]. It has been proposed that the genetic mechanisms for high Ba-Sr granitoids include the partial melting of subducted ocean plateau resulting from mafic high Ba-Sr magma underplating [16], partial melting of metasomatized lithospheric mantle by asthenosphere-derived carbonatitic [16] or continental slab-derived melts [19,20], partial melting of mafic lower crust involving enriched mantle-derived magmas [18,21], mixing of acid and basic magmas produced from lower crust and enriched mantle, respectively [22,23], and crystal fractionation from the associated enriched lithospheric mantle-derived alkaline magmas accompanied with minor crustal assimilation [24–26]. The variable origins of high Ba-Sr granitoids play an important role in revealing the tectonic evolution of orogenic belts [27].

Mesozoic giant igneous magmatism in Jiaodong Peninsula is one of the principal geological events closely associated with Palaeo-Pacific plate subducting [28,29]. In particular, the Cretaceous giant igneous magmatism was coincident with the shift of Palaeo-Pacific plate drifting [8]. Furthermore, it is noted that a great number of high Ba-Sr granitoids (c. 162–110 Ma) have been discovered in the Jiaobei terrane [30,31]. Therefore, the tectonic-magmatic processes of high Ba-Sr granitoids are the key to unravel the tectonic evolution in Jiaodong Peninsula associated with late Early Cretaceous Palaeo-Pacific plate subducting. However, the formation of the late Early Cretaceous magmas is still not well constrained [8]. Here, we analyze element compositions and Sr-Nd isotopes as well as zircon LA-ICP-MS U-Pb dating so as to illustrate the tectonic-magmatic processes of the late Early Cretaceous granitoids and offer new insight into the tectonic transition in the Jiaodong Peninsula.

2. Geological Setting and Sampling

The Jiaodong Peninsula, on the East China continental margin, is bounded by the Pacific Plate to the east and separated from the Luxi Block in NCC by the NNE-trending TLF to the west (Figure 1a,b) [6]. It can be separated into Sulu terrane in the southeast and Jiaobei terrane in the northwest based on the lithospheric-scale ENE- to NE-oriented WQYF [32,33]. The Jiaobei terrane basement rocks consist of Mesoarchean-Neoarchean Jiaodong Group TTG gneisses with Neoarchean amphibolites and mafic granulites [34,35], Palaeoproterozoic Jingshan and Fenzishan Groups, including metasedimentary marbles, calc-silicate rocks, and amphibolites [36,37] undergoing a c. 1.8 Ga amphibolite- to granulite-facies metamorphism [35,38], and the Neoproterozoic Penglai Group, consisting of slates, marbles and quartzites [39]. The crystalline basement in the Sulu terrane mainly includes Neoproterozoic and Palaeoproterozoic basement rocks of YC [40–42], which underwent a c. 244–220 Ma ultrahigh-pressure (UHP) metamorphic event [43,44]. Coesite-bearing eclogite, granitic gneiss, marble and quartzite composed the UHP metamorphic rocks [36,45], which were overprinted by the 220–205 Ma amphibolite to granulite-facies metamorphism locally [46]. The Palaeo-Pacific plate subduction resulted in the large scale Mesozoic magmatism in the Jiaodong Peninsula (Figure 1b) [8]. These Mesozoic magmatic rocks mainly occurred during two major episodes [47]: (a) Late Jurassic monzogranite and biotite granite (166–149 Ma) [3,48] and (b) Early Cretaceous (130–110 Ma) porphyritic-like monzogranite, granodiorite and syenogranite [49,50]. In addition, in the Jiaodong Peninsula, a great number of Mesozoic mafic dykes also occurred [51,52].

The Dazeshan granitic pluton, with an area of c. 25 km^2, intruding into the southwest part of the Late Jurassic Linglong batholith in Jiaobei terrane (Figure 1), is a sheet-like NE- to NNE-trending intrusive body (Figure 2a,b). It is composed of massive and homogeneous monzogranites, showing the sharp contact with the host rock (Figure 2c,d). These monzogranites are medium- to coarse-grained and light flesh-pink in appearance (Figure 2e) and generally show typically porphyritic-like texture with a large amount of megacrysts of K-feldspar (Figure 2e). In addition, microgranular dark enclaves occur

widely but are scarce (less than 1%) in these monzogranites (Figure 2f). They range from a few centimeters to decimeters in size (Figure 2f) and are oval to tabular in shape, commonly showing abrupt contacts with their host granitoids (Figure 2g,f). Some enclaves contain K-feldspar megacrysts (Figure 2h), suggesting that the granitic and mafic magmas were coeval. Samples for this paper, consisting of monzogranites and their dark enclaves, were collected from the Dazeshan granitic pluton, the locations of which are given in Figure 2b.

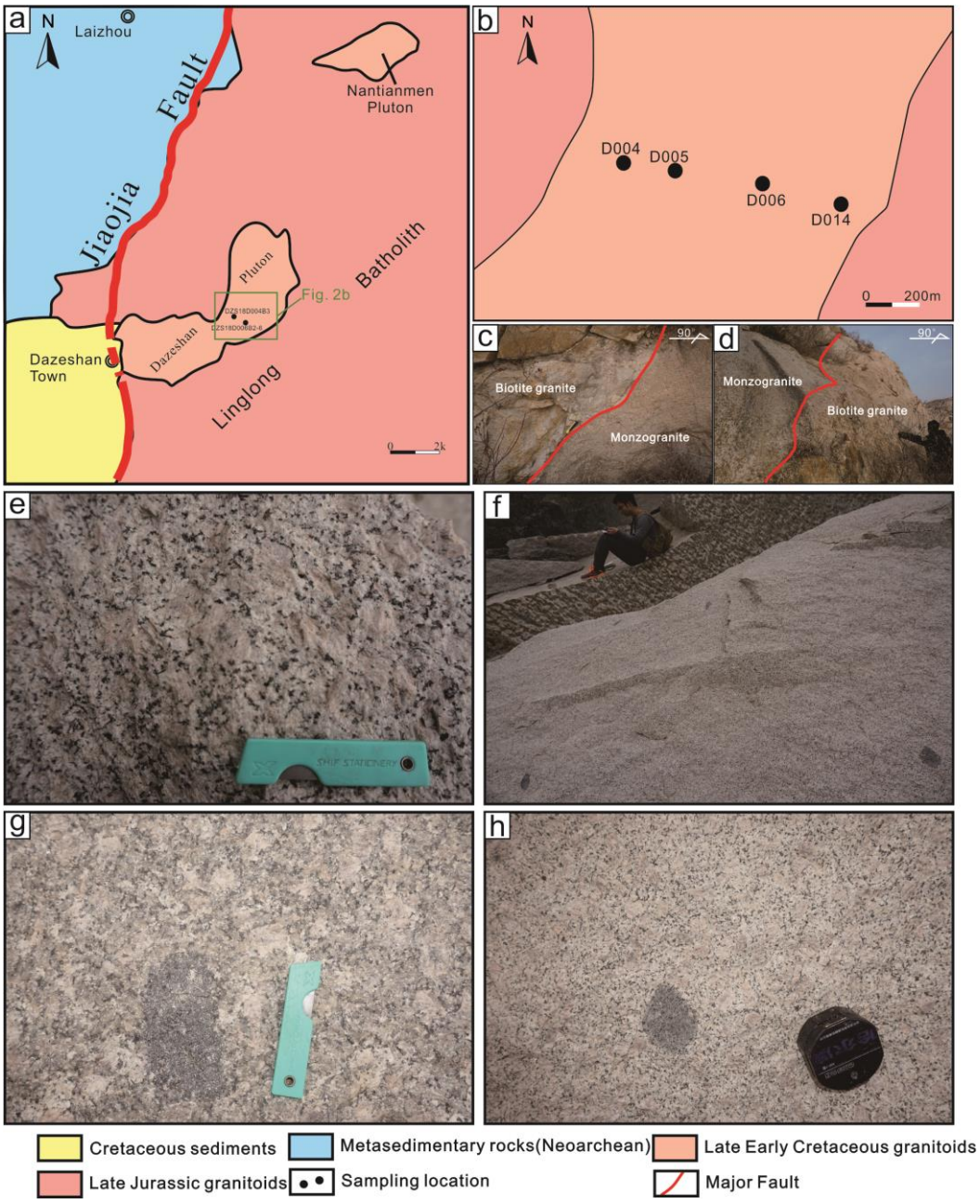


Figure 2. (**a**) Geological map of the Dazeshan pluton, illustrating its location and relation with Linglong batholith. (**b**) Enlarged geological map of Dazeshan granitoids illustrating sample locations. (**c**,**d**) Contact between fine-grained biotite granite and porphyritic-like monzogranite. (**e**) Porphyritic-like monzogranite with megacrysts of K-feldspar. (**f**) Dark microgranular enclaves in host monzogranites. (**g**) Tabular enclaves with abrupt contacts with their host. (**h**) Oval dark enclaves containing K-feldspar megacrysts.

The main mineralogy of monzogranite includes plagioclase (32–36%), K-feldspar (30–33%), quartz (22–25%), biotite (3–6%) and amphibole (<3%), with few accessory minerals of sphene, apatite and zircon (Figure 3a–c). K-feldspar is generally subhedral, with inclusions of biotite, plagioclase and quartz (Figure 3d). The dark enclaves are dioritic in composition and usually show fine-grained subhedral equigranular textures (Figure 3e,f). The minerals are mainly of plagioclase, hornblende and quartz, without or with K-feldspar and biotite, and the accessory minerals are apatite, zircon, magnetite and titanite (Figure 3f). No hydrothermal alteration and ductile structures are observed both in these granitoids and their dark enclaves (Figure 3).

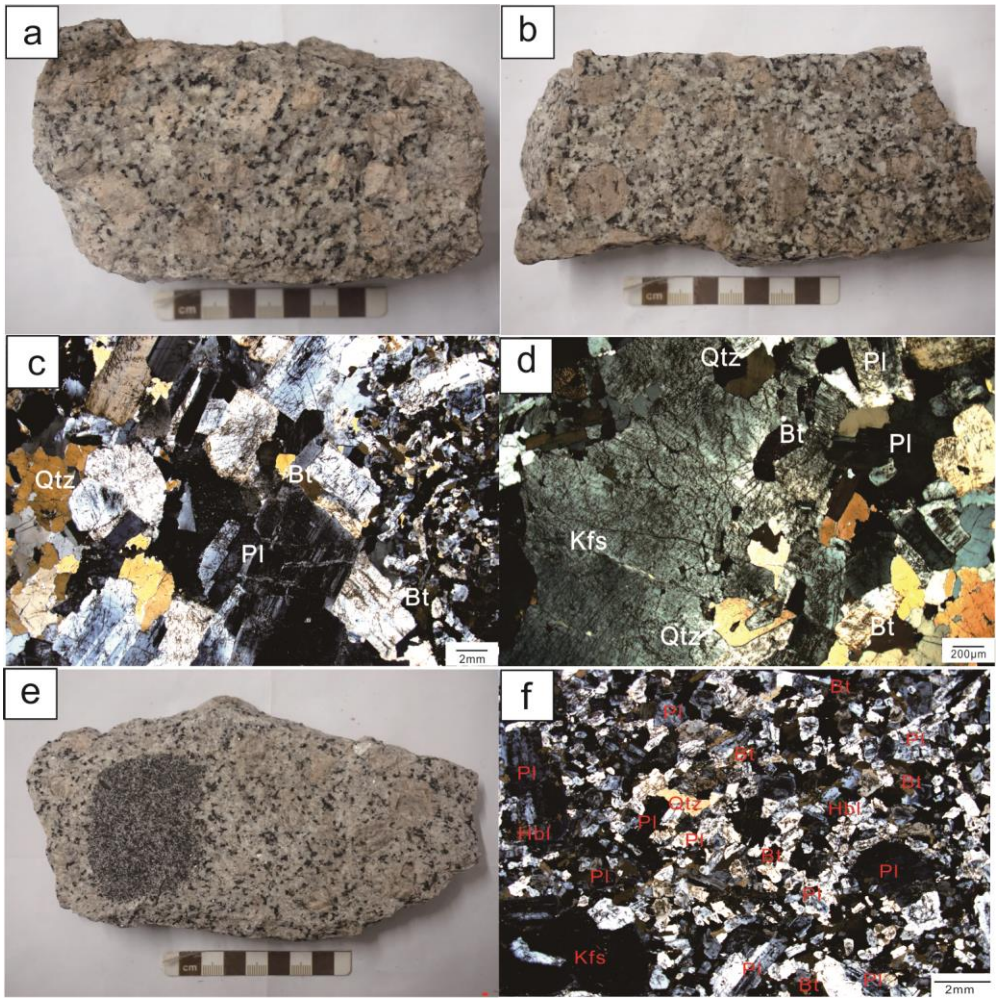


Figure 3. (**a**,**b**) Representative monzogranite samples for zircon LA-ICP-MS U-Pb dating and element analysis. (**c**) Euhedral to subhedral quartz, K-feldspar, plagioclase and biotite. (**d**) Subhedral K-feldspar with inclusions of biotite, plagioclase and quartz. (**e**) Representative fine-grained dark enclave sample for zircon LA-ICP-MS U-Pb dating and element analysis. (**f**) Fine-grained subhedral plagioclase, hornblende and quartz, K-feldspar and biotite. Mineral abbreviations: Pl: plagioclase, Qtz: quartz, Kfs: K-feldspar, Hbl: hornblende, Bt: biotite.

3. Analytical Methods

3.1. LA-ICP-MS Zircon U-Pb Dating

Over 500 zircon crystals were extracted from each sample after being crushed to c. 80–100 mesh for a grain size, using standard gravimetric-magnetic separation techniques at Langfang Technology Service Co., Ltd. of Geoscience Exploration, Hebei Province, China. Then, under a binocular microscope, at least 200 grains larger than 40 um in diameter containing no visible fractures and inclusions were handpicked, mounted in epoxy

resin and polished in order to expose the centre of zircon crystals. To choose the zircon grains without fluid/mineral inclusions and microcracks for U-Pb analyses, zircon internal textures were identified by examining the reflected and transmitted light micrographs in detail, which were obtained by optical microscopy at the geochemical research laboratory at China University of Geosciences (Beijing), as well as the cathodoluminescence (CL) images, which were obtained through a Quanta 200FEG environmental scanning electron microscope (SEM) at Beijing University.

Zircon U-Pb dating was performed by laser ablation inductively coupled plasma mass spectrometry (LA-ICP-MS) at the Hefei University of Technology, China, through an Agilent 7500a ICP-Mass furnished with a GeolasPro laser. The laser frequency was 6 Hz, and the spot diameter used for the analyse was 32 um. The external standard used as U-Pb dating was Harvard zircon 91500, and the external standard for calculating the contents of Th, U and Pb was NIST610. ICPMSDataCal 8.3 software was used to calculate the $^{206}Pb/^{238}U$ and $^{207}Pb/^{206}Pb$ ratios [53], and on the basis of the method of [54], we corrected the common Pb. The calculation of the weighted average ages and the concordia ages plotting were obtained using the Isoplot 4.16 program [55]. Detailed analytical techniques resembled those documented by [31,56].

3.2. Major- and Trace-Element Analyses

In this study, whole-rock major- and trace-element contents (including REEs) for twenty-one samples (sixteen monzogranites and five dark enclaves) were determined at the Research Institute of Uranium Geology, Beijing, China. The major elements were measured using a Philips PW2404 X-Ray Fluorescence Spectrometer (XRF), and the trace elements were determined by an ELEMENT-1 plasma mass spectrometer made by Finnigan-MAT Ltd. For major- and trace- elements, which included REEs, the analytical uncertainties were less than ±1% and ±5%, respectively. Ref. [57] introduced the detailed analytical procedures.

3.3. Whole Rock Sr and Nd Isotope Analyses

In this study, whole-rock Sr and Nd isotope analyses for twenty samples (sixteen monzogranites and four dark enclaves) were determined by a Finnigan MAT 262 multi-channel mass spectrometer at the Research Institute of Uranium Geology, Beijing, China. The powder (c. 110 –160 mg) of each sample was dissolved with the acid mixture of HNO_3 + HF (ratio of 1:2) in Teflon beakers. The separation of Sr and REEs was made through the combination of special Sr resin with standard cation-exchange columns. Then, the separation of Nd from the REEs was obtained through cation-exchange resin, with HIBA being eluent. The analytical procedures were introduced in detail by [58,59]. All the $^{143}Nd/^{144}Nd$ and $^{87}Sr/^{86}Sr$ fractionations measured were corrected according to the ratios of $^{143}Nd/^{144}Nd = 0.7219$ and $^{87}Sr/^{86}Sr = 0.1194$, respectively. During the analyses, the repeated analysis of the standard JNDi-1 for Nd produced $^{143}Nd/^{144}Nd = 0.512117 \pm 0.000005$ (2σ, n = 12), and the standard NBS-987 for Sr yielded $^{87}Sr/^{86}Sr = 0.710260 \pm 0.000010$ (2σ, n = 30). For Rb and Sr, total analytical blanks were (2–5) $\times 10^{-10}$ g, and they were 5×10^{-11} g for Sm and Nd.

4. Analytical Results

4.1. Zircon LA-ICP-MS U-Pb Age

The zircon LA-ICP-MS U-Pb isotope data obtained from the two monzogranite samples (DZS18D004B3 and DZS18D006B2-6) and one enclave sample (DZS18D004B1) are presented in Table 1. Figure 4 provides the U-Pb concordia age diagrams and histograms accompanied with the weighted average $^{206}Pb/^{238}U$ ages and the representative zircon cathodoluminescence (CL) images.

Table 1. LA-ICP-MS zircon U–Pb data of dark enclaves and host monzogranites of the Dazeshan pluton.

Spot	Concentrations (ppm)			Th/U	U–Pb Isotopic Ratios						Ages (Ma)					
	Pb	Th	U		$^{207}Pb/^{206}Pb$	1σ	$^{207}Pb/^{235}U$	1σ	$^{206}Pb/^{238}U$	1σ	$^{207}Pb/^{206}Pb$	1σ	$^{207}Pb/^{235}U$	1σ	$^{206}Pb/^{238}U$	1σ
DZSD04B3-01	7	255	292	0.9	0.052	0.004	0.133	0.011	0.019	0.00024	333	172	126	10	121	2
DZSD04B3-02	8	190	324	0.6	0.049	0.003	0.13	0.009	0.019	0.00023	167	−49	124	8	123	1
DZSD04B3-03	6	205	259	0.8	0.048	0.003	0.122	0.009	0.019	0.00027	122	143	117	8	120	2
DZSD04B3-04	11	296	449	0.7	0.049	0.003	0.126	0.007	0.019	0.00021	167	128	120	6	119	1
DZSD04B3-05	6	216	245	0.9	0.049	0.003	0.126	0.008	0.019	0.00027	200	133	121	7	121	2
DZSD04B3-06	10	320	385	0.8	0.049	0.003	0.128	0.007	0.019	0.00025	143	−64	123	7	122	2
DZSD04B3-07	12	312	462	0.7	0.049	0.002	0.124	0.006	0.018	0.00023	132	99	119	5	118	1
DZSD04B3-08	10	242	397	0.6	0.049	0.002	0.126	0.007	0.019	0.00023	128	−79	121	6	120	1
DZSD04B3-09	6	152	234	0.6	0.05	0.004	0.13	0.009	0.019	0.00031	176	163	124	8	123	2
DZSD04B3-10	10	261	410	0.6	0.05	0.003	0.127	0.008	0.019	0.00025	176	147	122	7	120	2
DZSD04B3-11	7	247	272	0.9	0.048	0.004	0.126	0.01	0.019	0.00027	102	185	120	9	121	2
DZSD04B3-12	7	267	288	0.9	0.046	0.006	0.115	0.015	0.018	0.00027	9	296	110	14	115	2
DZSD04B3-13	11	241	444	0.5	0.051	0.012	0.132	0.029	0.019	0.00074	228	456	125	26	122	5
DZSD04B3-14	23	130	175	0.7	0.049	0.009	0.692	0.119	0.102	0.00131	200	302	534	71	625	8
DZSD04B3-15	26	1301	859	1.5	0.05	0.007	0.13	0.019	0.018	0.0002	191	315	124	17	118	1
DZSD04B3-16	8	167	342	0.5	0.047	0.005	0.123	0.013	0.019	0.00027	32	222	118	12	120	2
DZSD04B3-17	6	165	272	0.6	0.046	0.004	0.117	0.01	0.019	0.00029	33	183	112	9	119	2
DZSD04B3-18	7	321	170	0.5	0.046	0.004	0.119	0.01	0.019	0.00028	30	18	114	9	120	2
DZSD04B3-19	38	287	266	1.1	0.067	0.003	0.927	0.035	0.1	0.00124	837	81	666	18	615	7
DZSD04B3-20	15	118	242	0.5	0.056	0.002	0.416	0.019	0.055	0.00183	435	87	353	14	345	11
DZSD04B3-21	5	116	221	0.5	0.053	0.003	0.133	0.008	0.019	0.0003	324	144	127	7	119	2
DZSD04B3-22	6	146	266	0.5	0.05	0.003	0.127	0.008	0.019	0.00031	189	145	122	7	119	2
DZSD04B3-23	11	278	484	0.6	0.05	0.002	0.131	0.005	0.019	0.00022	209	100	125	5	121	1
DZSD04B3-24	6	182	260	0.7	0.049	0.003	0.127	0.007	0.019	0.00033	128	126	121	6	121	2
DZSD04B3-25	56	382	499	0.8	0.066	0.002	0.742	0.019	0.081	0.00087	1200	49	564	11	502	5
DZSD06B2-6-01	20	126	129	1.0	0.067	0.002	1.03	0.032	0.113	0.0023	835	59	719	16	688	13
DZSD06B2-6-02	8	205	316	0.6	0.053	0.002	0.139	0.006	0.019	0.00027	345	102	132	5	122	2
DZSD06B2-6-03	8	262	312	0.8	0.049	0.003	0.126	0.007	0.019	0.00025	139	128	121	6	120	2
DZSD06B2-6-04	16	527	658	0.8	0.05	0.002	0.127	0.004	0.019	0.00018	195	75	122	4	118	1
DZSD06B2-6-05	8	182	339	0.5	0.047	0.002	0.122	0.006	0.019	0.00026	50	104	117	5	119	2
DZSD06B2-6-06	6	154	239	0.6	0.05	0.003	0.125	0.007	0.019	0.00036	187	146	120	6	119	2
DZSD06B2-6-07	9	217	385	0.6	0.05	0.003	0.126	0.006	0.019	0.00039	187	134	120	6	119	2
DZSD06B2-6-08	7	183	282	0.6	0.049	0.003	0.123	0.007	0.018	0.00038	154	133	118	6	117	2
DZSD06B2-6-09	5	163	187	0.9	0.051	0.004	0.119	0.009	0.018	0.00046	220	179	114	8	114	3
DZSD06B2-6-10	8	160	392	0.4	0.051	0.003	0.138	0.007	0.02	0.00035	228	122	132	7	125	2
DZSD06B2-6-11	6	128	245	0.5	0.052	0.004	0.133	0.008	0.019	0.00078	283	156	126	8	123	5
DZSD06B2-6-12	5	164	197	0.8	0.049	0.003	0.127	0.009	0.019	0.00035	154	168	121	8	118	2
DZSD06B2-6-13	8	182	336	0.5	0.047	0.003	0.12	0.007	0.018	0.00027	56	133	115	6	118	2
DZSD06B2-6-14	10	291	419	0.7	0.051	0.002	0.134	0.006	0.019	0.00027	250	106	128	5	122	2
DZSD06B2-6-15	9	155	286	0.5	0.046	0.003	0.117	0.007	0.019	0.00027	6	141	113	7	118	2
DZSD04B1-01	45	311	885	0.05	0.056	0.003	0.299	0.014	0.038	0.00054	471	100	266	11	241	3
DZSD04B1-02	22	1337	803	1.7	0.048	0.002	0.123	0.005	0.019	0.00027	100	89	117	5	118	2
DZSD04B1-03	62	4121	1652	2.5	0.142	0.063	0.119	0.037	0.019	0.00044	2252	852	114	34	122	3
DZSD04B1-04	31	1721	1054	1.6	0.053	0.003	0.142	0.009	0.020	0.00049	332	147	134	8	126	3
DZSD04B1-05	33	1908	1055	1.8	0.048	0.005	0.121	0.013	0.019	0.00082	122	231	116	12	119	5
DZSD04B1-06	4	152	171	0.9	0.049	0.007	0.120	0.017	0.018	0.00035	150	315	115	15	115	2
DZSD04B1-07	5	219	207	1.1	0.051	0.008	0.131	0.020	0.018	0.00036	239	315	125	18	117	2
DZSD04B1-08	30	1555	946	1.6	0.051	0.013	0.136	0.036	0.019	0.00022	232	513	129	32	123	1
DZSD04B1-09	13	939	640	1.5	0.047	0.007	0.121	0.018	0.019	0.00035	65	324	116	16	119	2
DZSD04B1-10	4	88	185	0.5	0.051	0.005	0.126	0.013	0.019	0.00038	243	230	121	12	119	2
DZSD04B1-11	39	1858	1362	1.4	0.046	0.002	0.120	0.006	0.019	0.0002	20	122	115	6	120	1

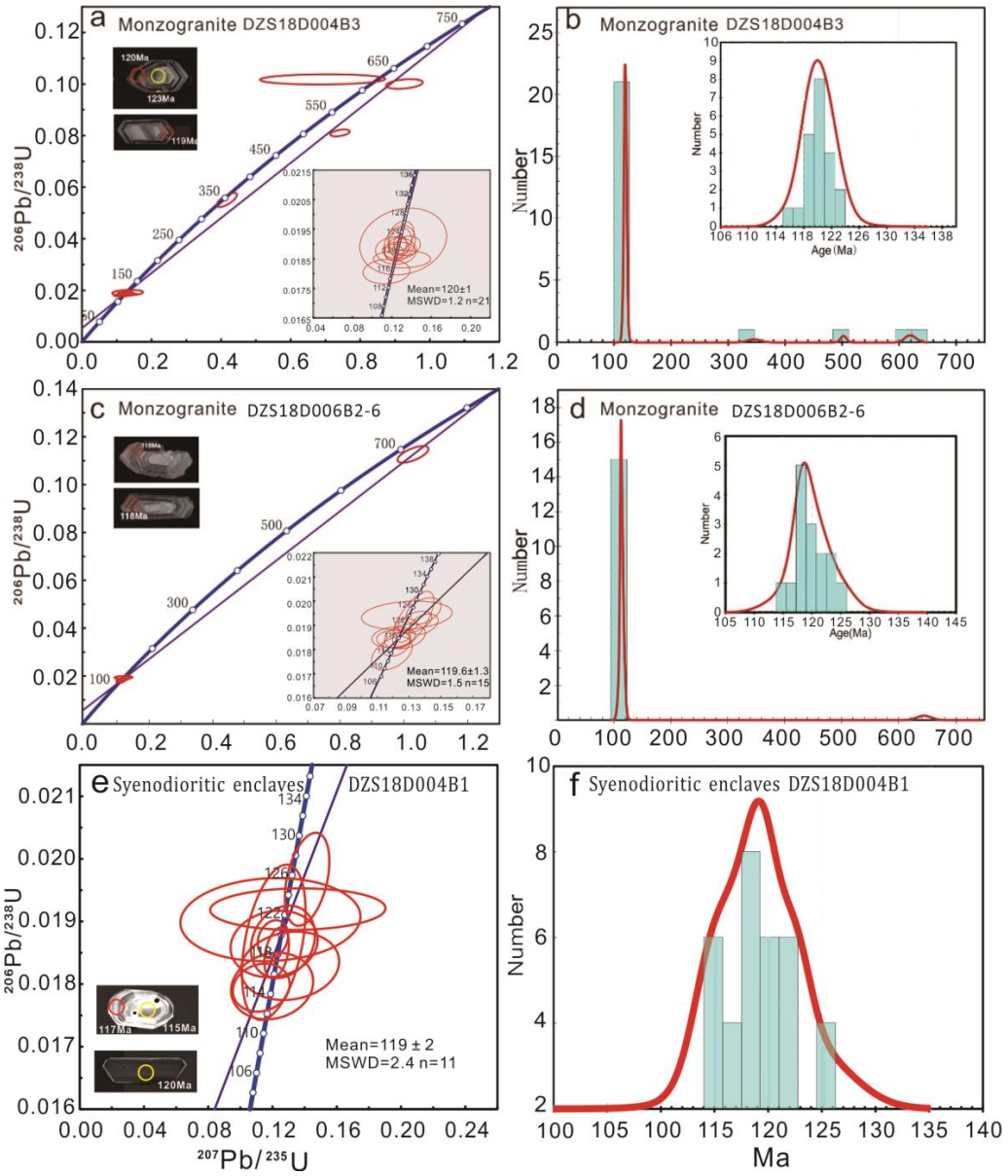


Figure 4. Zircon LA-ICP-MS U-Pb concordia age diagrams and histograms of Dazeshan monzogranites (**a**–**d**) and their enclaves (**e**,**f**). The insets show the typical zircon CL images with U-Pb apparent ages.

Zircons of both the monzogranites and their enclaves are prismatic and short, having length/width ratios and lengths of 1:1 to 3:1, and between 50 and 200 um, respectively. All the analyzed zircons are magmatic in origin as indicated by the oscillatory zoning shown on the CL images [60]. They have large variations in Th (88–4121 ppm) and U (129–1362 ppm) concentrations, with their Th/U ratios ranging between 0.4 and 2.5 (Table 1).

For monzogranite sample DZS18D004B3, we analyzed twenty-five zircon spots, which produced $^{206}Pb/^{238}U$ ages ranging between 115 ± 2 and 625 ± 8 Ma (Table 1; Figure 4a,b). Twenty-one of the twenty-five U-Pb isotopic data gave the concordant ages varying between 115 ± 2 and 123 ±2 Ma, with a weighted average age of 120 ± 1 Ma (2σ, MSWD = 1.2) (Figure 4a,b), and the four analyses of inherited zircons yielded the concordant ages between 345 ± 11 and 625 ± 8 Ma (Figure 4a,b).

Among the fifteen zircon spots performed for monzogranite sample DZS18D006B2-6, fourteen U-Pb isotopic data showed the concordant ages between 114 ± 3 and 125 ± 2 Ma,

with a weighted average age of 119.6 ± 1.3 Ma (2σ, MSWD = 1.5) (Table 1; Figure 4c,d), and the remaining one, having the old and concordant age at 688 ± 13Ma, was from inherited zircon (Figure 4d).

For the enclave sample (DZS18D004B1), the eleven zircon spots were analyzed, which gave concordant ages between 112 ± 3 and 134 ± 8 Ma, with a weighted average age of 119 ± 2 Ma (2σ, MSWD = 2.4) (Table 1; Figure 4e,f).

4.2. Whole-Rock Geochemistry

The major- and trace-element compositions for the monzogranites and their dark enclaves are shown in Figure 5 and Table A1. The rocks analyzed all have small loss on ignition (LOI) between 0.43% and 1.33% (Table A1), suggesting that these samples did not suffer any significant post-magmatic alteration, which is in accordance with the petrographic observations both in the field and from the thin sections (Figure 2).

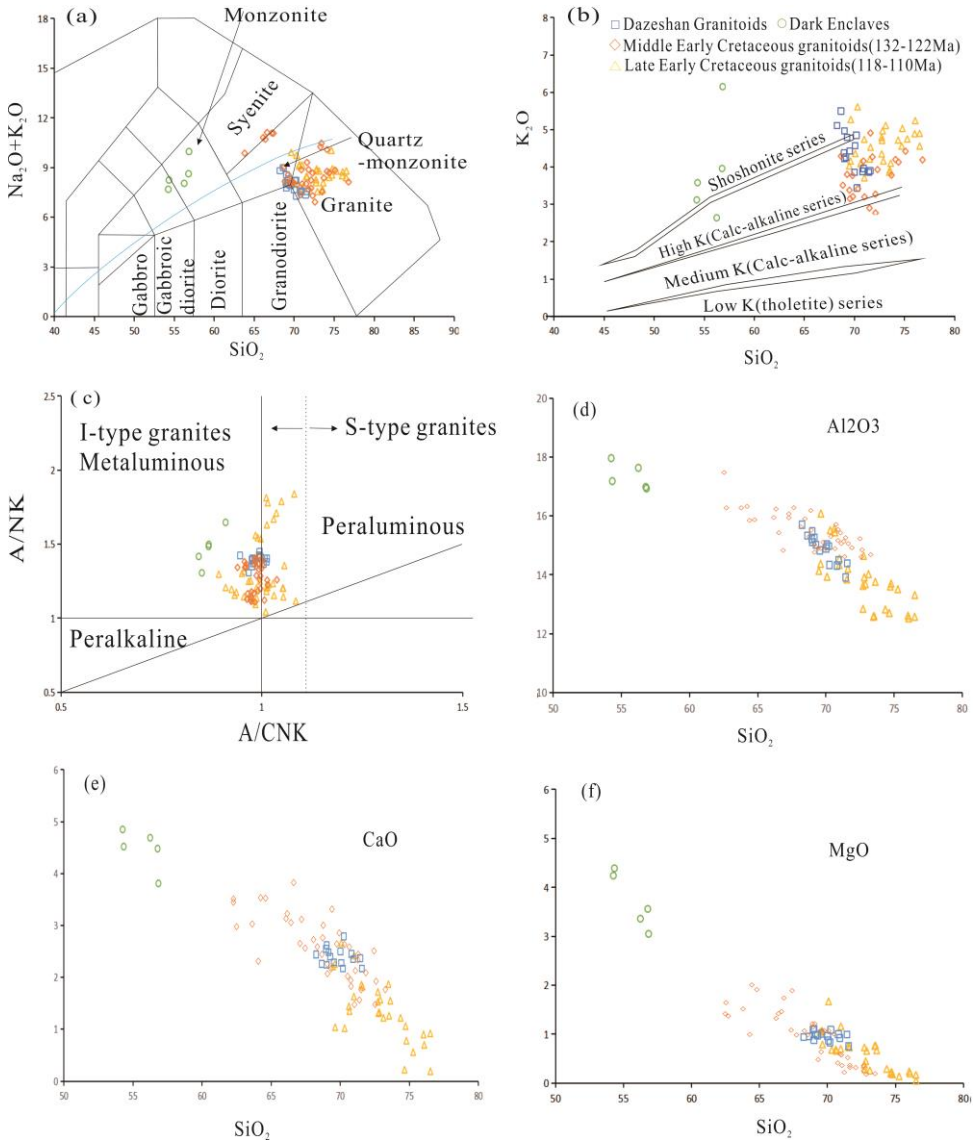


Figure 5. (**a**) Total alkali versus silica (TAS) diagram [61]. (**b**) K_2O vs. SiO_2 classification diagram [62]. (**c**) A/NK (molar $Al_2O_3/(Na_2O + K_2O)$) vs. A/CNK (molar $Al_2O_3/(CaO + Na_2O + K_2O)$) diagram [63]. (**d**–**f**) Harker variation diagrams show the correlations of Al_2O_3, MgO and CaO with SiO_2. The data for middle Early Cretaceous granitoids (132–122 Ma) [64–66] and Late Early Cretaceous granitoids (118–110 Ma) [49,50] previously published are also shown on the Figures.

Granitoids of the Dazeshan pluton are acidic in composition and have SiO_2 contents ranging from 68.25 wt.% to 71.56 wt.% (Table A1; Figure 5a). They show high total alkalis ($Na_2O + K_2O$ = 7.29–9.00 wt.%), mainly falling into the domain of the sub-alkaline monzogranite on the diagram of SiO_2 vs. ($Na_2O + K_2O$) (Figure 5a). These samples have relatively high K_2O concentrations of 3.44–5.50 wt.%, with K_2O/Na_2O of 0.89–1.57, and are in the domains of high-K calc-alkaline and shoshonite on the K_2O vs. SiO_2 diagram (Figure 5b) [62], indicating the overall potassic character (Figure 5b). They have a narrow range in contents of Al_2O_3 (13.91–15.70 wt.%), CaO (2.17–2.79 wt.%), TiO_2 (0.26–0.36 wt.%), TFe_2O_3 (1.98–2.69 wt.%) and P_2O_5 (0.10–0.161 wt.%) (Table A1). Based on the aluminum saturation index A/CNK (molar $Al_2O_3/(CaO + Na_2O + K_2O)$), granitoids of the Dazeshan pluton show metaluminous to weakly peraluminous character, with A/CNK of 0.94–1.01 (Figure 5c). All these analyzed granitoids have a very narrow range of low MgO concentrations (0.76–1.11%), with the Mg# molar 100*MgO/(MgO + FeO_T) of 40–43. Enclaves in the Dazeshan pluton, having the SiO_2 concentrations of 54.25–56.84 wt.%, are intermediate in composition and correspond to syenodiorite (Figure 5a). They have higher contents of TiO_2 (0.70–1.02 wt.%), Al_2O_3 (16.93–17.96 wt.%), TFe_2O_3 (6.86–8.65 wt.%), CaO (3.81–4.85 wt.%), P_2O_5 (0.45–0.67 wt.%) and MgO (3.05–4.39 wt.%), with a higher Mg# of 44–49 as compared those of the host granitoids (Table A1). These enclave samples have relatively high total alkalis concentrations of 7.69–9.97%, with variable K_2O contents of 2.64–6.15 wt.% and K_2O/Na_2O ratios of 0.49–1.61, showing alkaline and shoshonitic characteristics (Figure 5b), and they are metaluminous, having A/CNK of 0.84–0.91 (Figure 5c). For granitoids and their enclaves, the major oxides of MgO, Al_2O_3 and CaO concentrations generally have negative correlations with SiO_2 values (Figure 5d–f).

As shown in Table A1 and the chondrite-normalized REE diagrams (Figure 6a), both granitoids of the Dazeshan pluton and their enclaves are characterized by high total REE concentrations, with the ΣREE being 138–220 ppm and 359–572 ppm, respectively. Both are rich in LREE, with the ratios of $(La/Yb)_N$ varying between 32 and 50 for the granitoids and varying between 15 and 47 for the enclaves. The enclaves show moderate negative Eu anomalies, having Eu/Eu* values of 0.45–0.65 (Figure 6a), whereas the granitoids possess unclearly negative Eu anomalies (Eu/Eu* = 0.73–1.00), except that one sample has Eu/Eu* ratio of 0.66 (Figure 6a).

Granitoids of Dazeshan pluton are obviously rich in large ion lithophile element (LILE) concentrations, such as Rb (94–137 ppm), Sr (451–638 ppm) and Ba (1157–2842 ppm), with Rb/Sr and Sr/Y values of 0.18–0.27 and 50–79, respectively (Table A1; Figure 7a). The enclaves have Rb (162–220 ppm), Sr (387–544 ppm), Ba (629–1413 ppm), Rb/Sr (0.30–0.56) and Sr/Y (15–25) (Table A1; Figure 7a). Contents of HFSEs for the granitoids and their enclaves are Nb (6.9–9.7 and 15.6–31.4 ppm), Hf (0.47–1.10 and 1.55–1.89 ppm), Ta (0.63–0.88 and 1.09–2.95 ppm), Y(7.2–10.9 and 19.2–35.6 ppm) and Th (10–29 and 19–35 ppm), respectively. The enclaves show higher concentrations of compatible elements such as V (102–124 ppm), Ni (10–30 ppm) and Cr (12–133 ppm) than those of their host rocks, with V (21.4–44.8 ppm), Ni (4.51–7.04 ppm) and Cr (9.9–19.6 ppm). Both the enclaves and their host granitoids show strong negative Ta and Nb anomalies and positive Pb and K peaks on the primitive mantle-normalized spidergrams (Figure 7a).

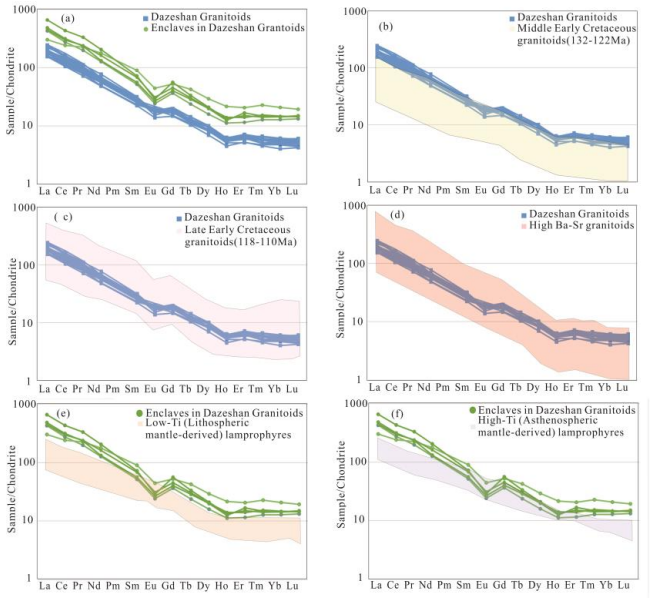


Figure 6. Comparison of chondrite-normalized REE patterns between granitoids of the Dazeshan and their enclaves (**a**), Dazeshan granitoids and middle Early Cretaceous granitoids (132–122 Ma) (**b**), Dazeshan granitoids and late Early Cretaceous granitoids (118–110 Ma) (**c**), Dazeshan granitoids and high Ba–Sr granitoids (**d**), Dark microgranular enclaves and low-Ti (Lithospheric mantle-derived) lamprophyres (**e**), and Dark microgranular enclaves and high-Ti (Asthenospheric mantle-derived) lamprophyres (**f**). The published data for middle Early Cretaceous granitoids (132–122 Ma) are from [64–66], for Late Early Cretaceous granitoids (118–110 Ma) from [49,50,67], for high Ba–Sr granitoids from [24], and for low-Ti and high-Ti lamprophyres from [47].

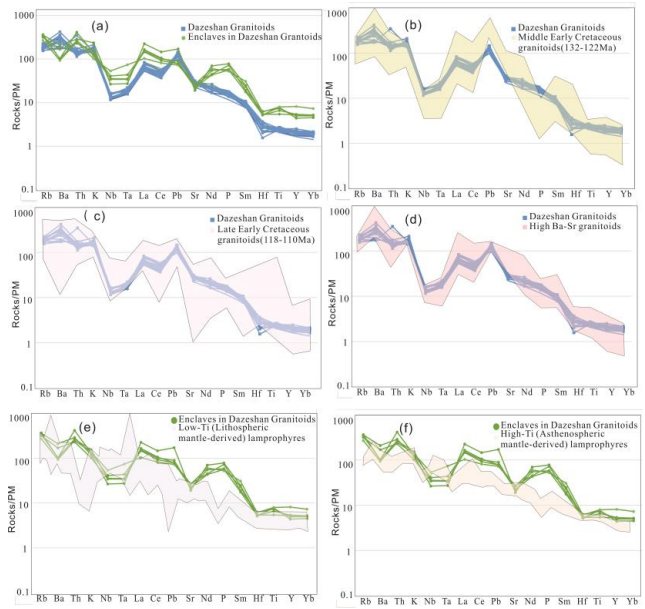


Figure 7. Comparison of primitive mantle-normalized spider diagrams between granitoids of the Dazeshan and their enclaves (**a**), Dazeshan granitoids and middle Early Cretaceous granitoids (132–122 Ma) (**b**), Dazeshan granitoids and late Early Cretaceous granitoids (118–110 Ma) (**c**), Dazeshan granitoids and high Ba–Sr granitoids (**d**), Dark microgranular enclaves and low-Ti (Lithospheric mantle-derived) lamprophyres (**e**), and Dark microgranular enclaves and high-Ti (Asthenospheric mantle-derived) lamprophyres (**f**). The published data for middle Early Cretaceous granitoids (132–122 Ma) are from [30,64–66], for Late Early Cretaceous granitoids (118–110 Ma) from [49,50,67], for high Ba–Sr granitoids from [24], and for low-Ti and high-Ti lamprophyres from [47].

4.3. Whole-Rock Sr-Nd Isotopes

Twenty representative samples (sixteen granitoids and four enclaves) were analyzed for Sr and Nd isotopic compositions in this study; they are listed in Table 2.

Granitoids of the Dazeshan pluton show $^{87}Sr/^{86}Sr$ ratios of 0.710638–0.710876 and $^{143}Nd/^{144}Nd$ values of 0.511434–0.511578, whereas their enclaves have slightly higher $^{87}Sr/^{86}Sr$ ratios of 0.711018–0.712482 and $^{143}Nd/^{144}Nd$ ratios of 0.511439–0.511633.

The initial $^{87}Sr/^{86}Sr$ ratios $(^{87}Sr/^{86}Sr)_i$ and εNd(t) values were obtained at 120 Ma according to the zircon LA-ICP-MS U-Pb dating for both granitoids and their enclaves in this study. The data are plotted in the diagram of εNd(t) vs. $(^{87}Sr/^{86}Sr)_i$ (Figure 8). Granitoids show a narrow range of $(^{87}Sr/^{86}Sr)_i$ ratios of 0.709361–0.709858, and strongly negative εNd(t) values of –21.6 to –18.8, with the two-stage Nd model ages (T_{DM2}) varying between 2449 and 2679 Ma, consistent with those of their enclaves, with $(^{87}Sr/^{86}Sr)_i$ = 0.709523–0.709726, εNd(t) = –21.8 to –17.8 and T_{DM2} = 2365–2691 Ma.

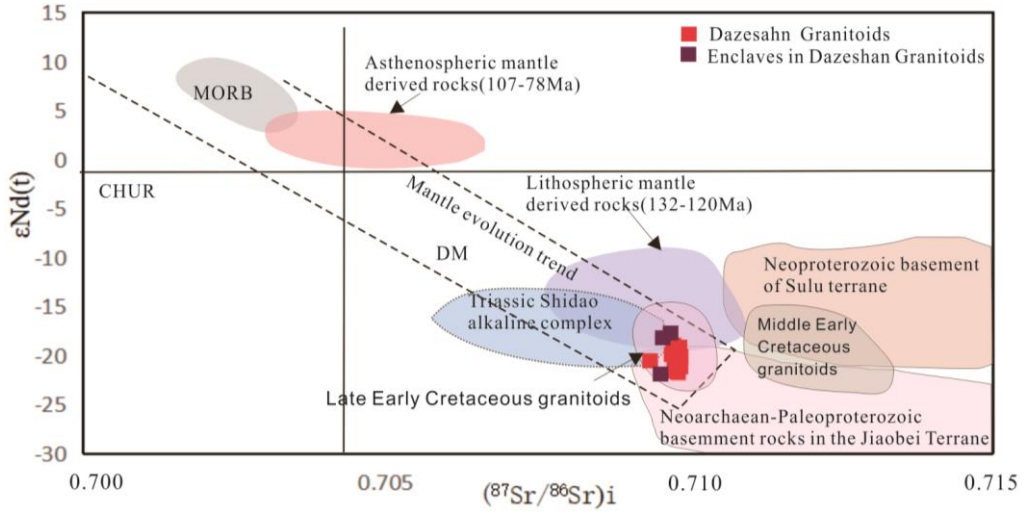


Figure 8. $(^{87}Sr/^{86}Sr)_i$ vs. εNd(t) diagram for Dazeshan granitoids and their enclaves. Data sources: MORB [68]; Mafic dikes derived from lithospheric mantle (132–120 Ma) from [28,47,69]; Mafic rocks derived from asthenospheric mantle (107–78 Ma) from [34,70]; Neoarchaean-Neoproterozoic basement rocks in the Jiaobei Terrane from [71]; Neoproterozoic basement rocks in the Sulu Terrane from [38]; Triassic Shidao alkaline complex from [72]. CHUR: chondritic uniform reservoir; MORB: middle ocean ridge basalt; DM: depleted mantle.

Table 2. Rb-Sr and Sm-Nd isotopic results of host granitoids and dark enclaves from the Dazeshan pluton.

Sample	Rock Type	Rb (ppm)	Sr (ppm)	$^{87}Rb/^{86}Sr$	$^{87}Sr/^{86}Sr$	$\pm 2\sigma$	$(^{87}Sr/^{86}Sr)_i$	Sm (ppm)	Nd (ppm)	$^{147}Sm/^{144}Nd$	$^{143}Nd/^{144}Nd$	$\pm 2\sigma$	εNd(t)	T_{DM2} (Ma)	T_{DM} (Ma)
DZSD04B1	Monzo-granite	108	593	0.52736054	0.710714	0.000019	0.709814612	4.17	30.3	0.083201822	0.511434	0.000018	−21.75	2679	2000
DZSD04B2-1		122	594	0.594719192	0.710737	0.000016	0.709722735	3.92	26.7	0.088759371	0.511535	0.000015	−19.87	2527	1967
DZSD04B2-2		137	638	0.621782445	0.710838	0.000016	0.709777579	4.22	28	0.091115829	0.511504	0.000009	−20.51	2579	2042
DZSD04B3		113	638	0.512857053	0.710657	0.000016	0.709782347	3.75	25	0.090684	0.511538	0.000021	−19.84	2525	1993
DZSD05B1		133	590	0.652736949	0.710876	0.000014	0.709762788	3.39	22.2	0.092317946	0.511468	0.000011	−21.23	2637	2107
DZSD06B2-1		127	602	0.610865781	0.710791	0.000014	0.709749197	4.66	34.9	0.080723484	0.511566	0.00001	−19.14	2468	1813
DZSD06B2-2		122	632	0.558960759	0.710741	0.000013	0.709787719	3.85	26.7	0.087174382	0.511537	0.000009	−19.81	2522	1939
DZSD06B2-3		106	601	0.510704825	0.710638	0.000021	0.709767017	3.67	25	0.088749408	0.511558	0.000009	−19.42	2491	1937
DZSD06B2-4		123	632	0.563542405	0.710739	0.000011	0.709777905	4.51	30.8	0.088524857	0.511542	0.00001	−19.73	2516	1954
DZSD06B2-5		131	609	0.622863054	0.710777	0.000016	0.709714737	4.02	26.6	0.091365835	0.511538	0.000008	−19.85	2526	2005
DZSD06B2-6		95	523	0.525969407	0.710666	0.000016	0.709768984	4.36	30.3	0.086992792	0.511529	0.00001	−19.96	2534	1946
DZSD14B1-1		108	555	0.563468108	0.710799	0.000018	0.709838032	4.14	29.4	0.085131918	0.511565	0.000013	−19.23	2475	1876
DZSD14B1-2		122	451	0.783288692	0.710697	0.000014	0.709361138	3.28	21.8	0.090961321	0.5115	0.000018	−20.59	2585	2044
DZSD14B1-3		94.4	486	0.562437531	0.710742	0.000016	0.709782789	4.19	28	0.090468086	0.511552	0.000017	−19.56	2502	1973
DZSD14B1-4		101	564	0.518538298	0.710742	0.000021	0.709857657	3.97	26	0.092311662	0.511524	0.000007	−20.14	2549	2037
DZSD14B1-5		105	553	0.549797468	0.710677	0.000016	0.709739346	4.16	31.2	0.080608	0.511578	0.000006	−18.91	2449	1798
DZSD04B1(bt)	enclaves	202	454	1.288350661	0.71174	0.000014	0.709542779	7.6	57.3	0.080185969	0.511614	0.000007	−18.20	2392	1751
DZSD04B2-1(bt)		162	535	0.876798505	0.711018	0.000016	0.709522662	13.2	80.1	0.099627865	0.511439	0.000014	−21.91	2691	2280
DZSD04B2-2(bt)		191	442	1.251266063	0.711792	0.000011	0.709658025	9.99	72.8	0.082960912	0.511633	0.000011	−17.87	2366	1766
DZSD05B1(bt)		216	387	1.616148837	0.712482	0.000017	0.709725735	10.60	92.6	0.069204492	0.51147	0.000006	−20.84	2605	1770

Note: $\varepsilon Nd = [(^{143}Nd/^{144}Nd)_S/(^{143}Nd/^{144}Nd)_{CHUR} - 1] \times 10000$, $f_{Sm/Nd} = (^{147}Sm/^{144}Nd)_S/(^{147}Sm/^{144}Nd)_{CHUR} - 1$, $t_{DM2} = (1/\lambda_{Sm})\ln(1 + A)$, $A = \{(^{147}Sm/^{144}Nd)_S - (^{147}Sm/^{144}Nd)_{DM} - [(^{147}Sm/^{144}Nd)_S - (^{147}Sm/^{144}Nd)_C]\ (e^{\lambda t} - 1)\}/[(^{147}Sm/^{144}Nd)_C - (^{147}Sm/^{144}Nd)_{DM}]$, $(^{147}Sm/^{144}Nd)_{DM} = 0.2136$, $(^{147}Sm/^{144}Nd)_{DM} = 0.513151$, $(^{147}Sm/^{144}Nd)_{CHUR} = 0.1967$, $(^{143}Nd/^{144}Nd)_{CHUR} = 0.512638$, $(^{147}Sm/^{144}Nd)_C = 0.118$, t = crystallization age of zircon (120Ma), $\lambda_{Sm} = 6.54 \times 10^{-12}$ year.

5. Discussion

5.1. Petrological Classification and Petrogenesis

As mentioned above, the large scale Early Cretaceous intrusive rocks (130–110 Ma) occurred in the Jiaodong Peninsula (Figure 1) [8,33,49]. Based on the lithology, geochemistry and geochronology, as well as their attitudes and spatial relationships, they can be traditionally divided into two subgroups [33,49,65,73]: (a) the middle Early Cretaceous granitoids (132–122 Ma), mainly consisting of quartz monzonite, granodiorite and porphyritic-like monzogranite, and trending E–W to ENE (Figure 1b); and (b) the late Early Cretaceous granitoids (118–110 Ma), mainly including porphyritic-like monzogranites, granodiorite and syenogranites, and trending NE to NNE (Figure 1b). The LA-ICP-MS zircon U-Pb ages obtained in this study provide the first precise geochronology on granitoids of the Dazeshan pluton and show ages of 119.6 ± 1.3 to 120 ± 1 Ma, which are between those of middle Early Cretaceous granitoids and late Early Cretaceous granitoids. Given that the granitoids in this study have the same petrology (Figure 3), attitude (Figure 1b), major-element composition (Figure 5), and REE and trace-element distribution patterns as those of the late Early Cretaceous granitoids (Figures 6 and 7), it is logical to infer that the Dazeshan pluton belongs to the late Early Cretaceous granitoids, and the crystallization age of c. 120 Ma probably represents the lower limit of emplacement ages for the late Early Cretaceous granitoids in the Peninsula. In addition, the LA-ICP-MS zircon U-Pb age of 119 ± 2 Ma obtained for the dioritic microgranular enclaves is the same as those of the host granitoids (119.6 ± 1.3 to 120 ± 1 Ma), suggesting that the felsic and intermediate magmas were coeval.

All the analyzed samples for granitoids of the Dazeshan pluton and their enclaves produced very low LOI (0.42–1.33 wt.%), as well as low La/Th ratios (1.0–6.4) and low to medium K/Sr ratios (49–160), suggesting that their element composition was not modified by the element migration [74,75]; therefore, all the major- and trace-element data obtained can be used to interpret their petrogenesis.

All the samples for granitoids of the Dazeshan pluton in this study have higher alkali contents ($Na_2O + K_2O$ = 7.29–9.00%), and lower Al_2O_3 (13.91–15.70%) and MgO values (0.76–1.11%) (Table A1; Figure 5) and flatter HREE patterns (Figure 7a) as compared to the calc-alkaline geochemical features that the typical adakitic rocks possess. In addition, they reflect a dominant calc-alkaline trend in the Na-K-Ca plot, instead of the trondhjemitic affinities of the adakitic rocks (Figure 9a). Furthermore, they show high Ba (>629 ppm), Sr (>451 ppm), K/Rb (>320) and LREEs (>132 ppm), as well as low Rb (<137 ppm), Th (<29 ppm), U (<2.4 ppm), Nb (<9.7 ppm), Ta (<0.9 ppm), Y (<10.9 ppm) and HREEs (<9.6 ppm) (Table 2), have no clearly negative Eu anomalies (Figure 6a) and are depleted in Nb in spidergrams (Figure 7a), which separate them from the traditional A-, M-, S- and I-type granites.

However, the very high Sr (451–638 ppm) and Ba (1157–2842 ppm) contents indicate Dazeshan granitoids are similar to the high Ba-Sr granitoids proposed by [16], which are characterized by high Sr (>300 ppm) and Ba (>500 ppm) concentrations. Based on the difference in Sr and Ba contents, in the Sr-Rb-Ba plot, all the analyzed Dazeshan granitoids plot inside the domain of the high Ba-Sr granite [16], which is different from the low Ba-Sr granite (Figure 9b). Furthermore, the lack of clearly negative Eu anomalies (Figure 6a), the apparent fractionated REE patterns (Figure 6a) as well as the prominent depletion in Ti, P, Nb and Ta (Figure 7a), together with the very low Yb and Y concentrations against high $(La/Yb)_N$ (32–50) and Sr/Y (50–79) ratios, are also similar to the typical geochemical characteristics of high Ba-Sr granitoids (Figures 6d and 7d) [20,76]. Therefore, it is logical to classify the Dazeshan granitoids as high Ba-Sr granitoids.

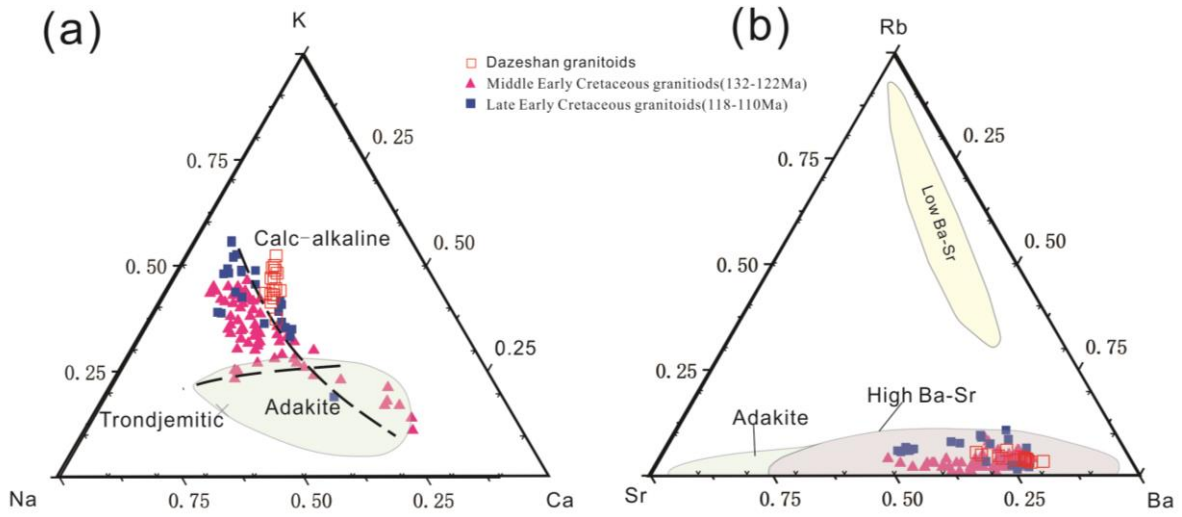


Figure 9. (**a**) Na-K-Ca and (**b**) Sr-Rb-Ba plots for the Dazeshan granitoids based on [16]. The published data for middle Early Cretaceous granitoids (132–122 Ma) [64–67] and Late Early Cretaceous granitoids (118–110 Ma) [49,50,68] are also shown in the Figures. Fields of low-Ba–Sr and high-Ba–Sr granitoids are from [76], and the field of adakite is from [17].

It was proposed that late Early Cretaceous granitoids (118–110 Ma) in the Jiaodong Peninsula resulted from the partial melting of continental lower-middle crust followed by crystal fractionation [65]. The microgranular dark enclaves were widely developed in late Early Cretaceous granitoids, such as Sanfoshan pluton [30], Yashan pluton [65], Changshannan pluton [64], Gushan pluton [66] and Weidesan plutons [77], which were considered to be a result of magma mixing between crust-derived and mantle-derived magmas [30,64–66,77]. Likewise, the microgranular dark enclaves were also observed in the Dazeshan pluton in this study. However, all the dark enclaves are dioritic, with SiO_2 concentrations of 52.46–58.06 wt.% (Figure 5a) [64–66,77], and they have negative εHf (t) values ranging from –19.6 to –16.1 [78], indicating a crustal derivation for these dark enclaves, although a mantle origin followed by the crustal contamination remains a possibility [79]. Furthermore, the indistinguishable $(^{87}Sr/^{86}Sr)_i$ values for the dark enclaves and their host granitoids (Table 2; Figure 8) suggest a cogenetic origin, which may be associated with a common evolution process, such as restite unmixing, crystal accumulation, crystal fractionation or liquid immiscibility, instead of the magma mixing, co-mingling or wall-rock assimilation models [47,52,79–85].

However, the primary igneous rather than metamorphic textures of the enclaves from the Dazeshan pluton (Figure 3) preclude an origin resulting from restite unmixing [69,81,84,86]. In addition, the much higher REE, Zr, Nb and P concentrations in the dark enclaves than those in their host granitoids (Table A1; Figures 6 and 7) rule out their relation to fractional crystallization [80,82,87,88]. Furthermore, a crystal accumulation model is also eliminated because of the greater REE and the moderately negative Eu anomalies (Eu/Eu* = 0.45–0.65) in contrast to the positive Eu anomaly shown in the dark enclaves (Table A1; Figure 6) [79,89,90]. Thus, it seems that liquid immiscibility is a viable model to explain the origin of the Dazeshan granitoids and their dark enclaves, which is also supported by the major-, trace-, and REE-element composition presented below, except for their identical $(^{87}Sr/^{86}Sr)_i$ values (Table 2; Figure 8).

Experimental studies show that silicate melts rich in MgO, CaO, P_2O_5, FeO and TiO_2 tend to split into one immiscible liquid pair, consisting of a quartzo-feldspathic acid liquid and an iron-rich intermediate-basic liquid, producing a gap in SiO_2 composition with a linear trend on the oxide against SiO_2 plots [91–94]. On a Greig pseudoternary phase diagram [SiO_2-(CaO + MgO + TFe_2O_3 + TiO_2 + P_2O_5)-(Na_2O + K_2O + Al_2O_3)], the Dazeshan granitoids and dark enclaves plot within a two-liquid immiscible field (Figure 10). In addition, they show a gap between 56.84 wt.% and 68.25 wt.% in SiO_2 composition, and

the oxides have a decreasing trend against SiO_2 increasing (Figure 5). Thus, the major-element compositional variation between the Dazeshan granitoids and dark enclaves could be related to a liquid immiscible process.

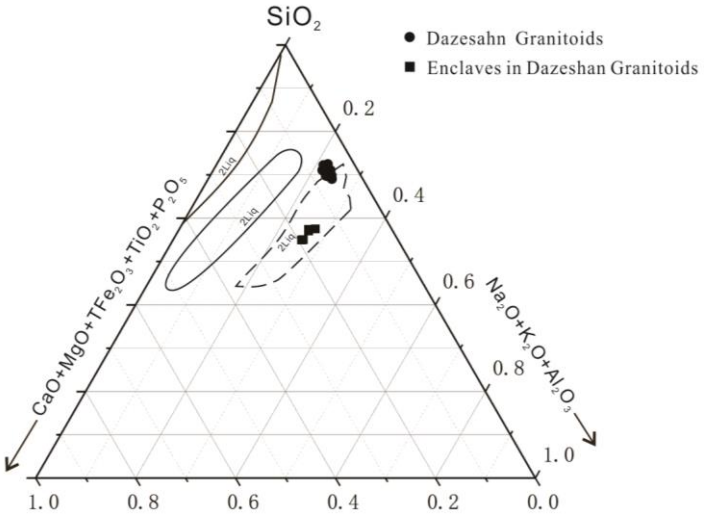


Figure 10. Plots for the Dazeshan granitoids and their enclaves on the Greig diagram. Fields for liquid immiscibility are from [80,95].

Furthermore, the relative contents of trace and REE elements in the silicic rocks and their dark enclaves can also be used to judge if they were derived from a liquid immiscible process [80,87,93,94]. In this study, the concentration of each trace element in the granitoid (acid material) was divided by that in the corresponding dark enclave pair (intermediate material). The distributions of resulting ratios are shown in Figure 11, which agree well with the distribution fields defined by the experimental two-liquid partitioning coefficients of [93,94], as well as the elemental rations between the acid and intermediate-basic materials that indicate one immiscible liquid pair [80,89,96]. In addition, it was suggested that the two immiscible liquids could have parallel REE distribution patterns, whereas REE abundances in immiscible intermediate-basic liquids are much greater than those in acid liquids [80]. It can be found that the REE distribution patterns between the Dazeshan granitoids and their enclaves are markedly parallel, and the dark enclaves have much greater rare earth element (REE) and HFSE abundances than those of their host granitoids, which is similar to those for the Rosetown diorite and granodiorite, representing two immiscible end-member liquids [80]. Therefore, it is logical to suggest that liquid immiscibility is a viable model to explain the chemical compositional variations between the Dazeshan granitoids and their dark enclaves.

It was suggested that the dioritic enclaves formed before and during liquid immiscibility are characterized by the typical textural features of distorted angular shapes with inward pointing cusps on their edges [80,97]. Hence, the spherical to tabular shape for the dark enclaves, which are lack of the inward pointing cusps, trapped in the Dazeshan granitoids may indicate the two immiscible end-member liquids during separation would have been almost free of crystals. Thus, the compositions of Dazeshan granitoids and their enclaves may represent those of the original melts. However, given the scarce dark enclaves in the Dazeshan granitoids, though they are widely distributed, the dioritic liquid could be an infinitesimal fraction compared to the parent; therefore, the acid liquid will have the composition approximating that of the parent magma.

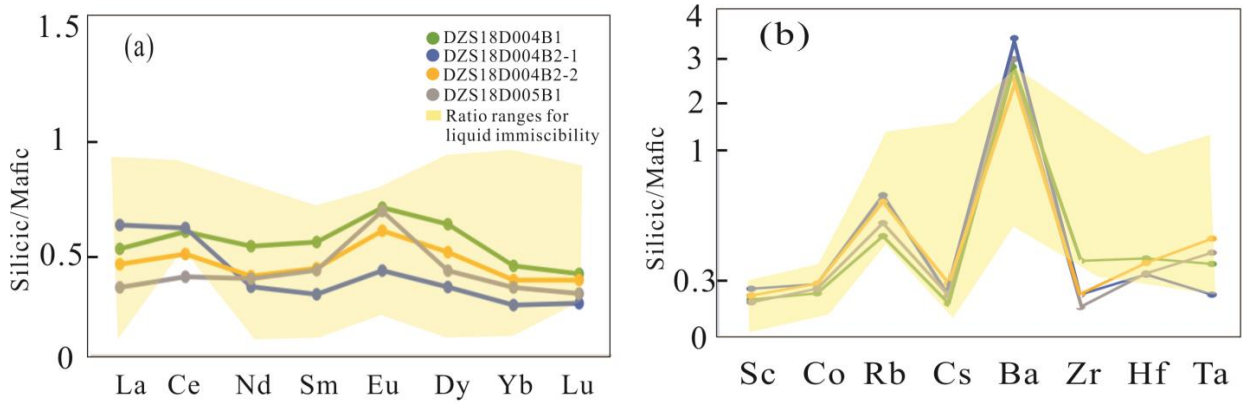


Figure 11. Ratios of REE elements (**a**) and trace elements (**b**) in dark enclaves to their corresponding host granitoids. Ranges for ratios of REE elements (**a**) and trace elements (**b**) in silicic liquid to those in mafic liquid are based on data from [80,89,93,94].

All the samples of Dazeshan granitoids studied show great SiO_2 (>68.25 wt.%) and low MgO (<1.11 wt.%), TiO_2 (0.26–0.36 wt.%) and TFe_2O_3 (1.98–2.69 wt.%) concentrations (Table A1; Figure 5), as well as high $(^{87}Sr/^{86}Sr)_i$ values (0.709361–0.709858) and highly negative εNd(t) values of –21.6 to –18.8 (Table 2; Figure 8), indicating their derivation from strongly evolved or crust-involved magmas. However, the almost homogeneous major and trace element concentrations within all the Dazeshan granitoids studied (Table A1), which is consistent with the petrographical homogeneity of the granitoids, as well as the insignificant negative Eu anomalies (Figure 6), suggest that no significant fractionation occurred during magma evolution. In addition, their T_{DM2} ages vary from 2449 to 2679 Ma (Table 2), in accordance with the ages of Neoarchean-Palaeoproterozoic amphibolite- to granulite-facies basement rocks in the Jiaobei terrane, reflecting a derivation from an ancient crust. Nevertheless, the enrichment in LILE and LREE but depletion in HFSE (Figure 6), the highly positive anomaly in Pb accompanied by the strong negative Nb, Ta, P and Ti anomalies (Figure 7), as well as the low Ce/Pb ratios of 2.22–5.82 (Table A1), suggest that the granitic magmas are likely generated from the partial melting of continental crust, related to an existing subduction event.

It was suggested that the mafic to felsic granulite, constituting the Archean-Proterozoic lower crust in the NCC, typically shows low K_2O (average 0.8 wt.%), Rb (average 16.4 ppm), Sr (average 232 ppm) and Ba (average 193 ppm) and is strongly depleted in Zr, U and Th as well as rich in Hf [41,98]. However, all these features contradict those shown in the Dazeshan granitoids studied here. Thus, it is impossible that the NCC Archean lower crust is the exclusive or direct source for these granitoids. Furthermore, the melting of the mafic to felsic granulite rocks need high melting temperatures [85,99]. In addition, the middle Early Cretaceous granitoids (132–122 Ma), which have higher SiO_2 (>70.89 wt.%) and lower MgO (<0.62 wt.%) concentrations, and higher $(^{87}Sr/^{86}Sr)_i$ values (0.71071–0.71172), were suggested to be derived from the mingling of the felsic melts, produced by the partial melting of Precambrian basement rocks of the Jiaobei terrane, with the intermediate magmas generated by the partial melting of juvenile mafic lower crust [100]. Therefore, it was proposed that Dazeshan granitoids are products of partial melting of the continental lower crust containing subduction-related materials induced by the injection of mantle-derived basic magmas. However, given the very low MgO concentrations and relatively high $(^{87}Sr/^{86}Sr)_i$ combined with the lack of any significant fractionation, it is suggested that likely only a few melts or mainly fluids came from the mantle, which is in accordance with the small portion of dark enclaves presented in the Dazeshan granitoids.

In the Jiaodong Peninsula, two types of coeval lamprophyres, i.e., low-Ti and high-Ti lamprophyres, were identified to be emplaced at c. 121 Ma. The low-Ti lamprophyres have high SiO_2 concentrations of 49.5–53.9 wt.% and high Mg# (63–74), and show enrichment in both LILEs and LREEs but high depletion in HFSEs, with strongly negative anomalies

in Zr, Hf, Nb, Ti and Ta (Figures 6e and 7e). They possess highly negative εNd(t) values (–13.9 to –15.5) and εHf(t) values (–23.1 to –19.3) and are considered to originate from an enriched subcontinental lithospheric mantle that was metasomatized by subduction-related fluids [47]. The high-Ti lamprophyres have low SiO_2 concentrations of 46.9–49.2 wt.% and Mg# (51–58) and show enrichment in LREEs, but lack Nb-Ta depletion and LILE enrichment (Figures 6f and 7f). They possess higher εNd(t) values (–0.79 to 1.76) and εHf(t) values (–4.7 to 2.1) and are considered to originate from an asthenospheric mantle unaffected by subduction-related materials [47]. The elemental and isotopic compositions of the dark enclaves in the Dazeshan granitoids are much closer to those of enriched subcontinental lithospheric mantle beneath the Jiaodong Peninsula as indicated by low-Ti lamprophyres (Figures 6e, 7e and 8), distinct from those of asthenospheric mantle-derived high-Ti lamprophyres in the Jiaodong Peninsula (Figures 6f, 7f and 8). Therefore, it is most likely the enriched subcontinental lithospheric mantle is the source for the mantle-derived materials.

Given the very small variations in major- and trace-element contents, such as SiO_2 (68.25–71.56 wt.%), Al_2O_3 (13.91–15.70%), CaO (2.17–2.79%), Y (7.2–10.9 ppm) and Yb (0.66–1.00 ppm), and the narrow ranges of $(La/Yb)_N$ ratios (32–50) for the Dazeshan granitoids, it is suggested that the crust-derived materials were likely from almost the same depth. Combined with the lack of both Neoarchean to Palaeoproterozoic inherited zircons and metamorphic wall rock enclaves in the Dazeshan granitoids and their dark enclaves, which are common in Late Jurassic (166–149 Ma) and middle Early Cretaceous granitoids (132–122 Ma), it is most likely that almost all the crust-derived components contained in the region of the magma source were melted, except for few Neoproterozoic to Palaeozoic inherited zircons, indicating their melting at higher crustal levels, likely due to the removal of the Archean lithospheric mantle as a consequence of delamination (Figure 12) [29,65]. In addition, the Dazeshan granitoids show the homogeneous Sr–Nd isotopic compositions, as are also indicated by other late Early Cretaceous granitoids (118–110 Ma), including the Changshannan pluton [64] and Gushan pluton [66]. Therefore, magma homogenization could have been obtained in the magma chamber at the crust base, and a MASH (melting, assimilation, storage, and homogenization) process [101] was responsible for the Dazeshan granitoids.

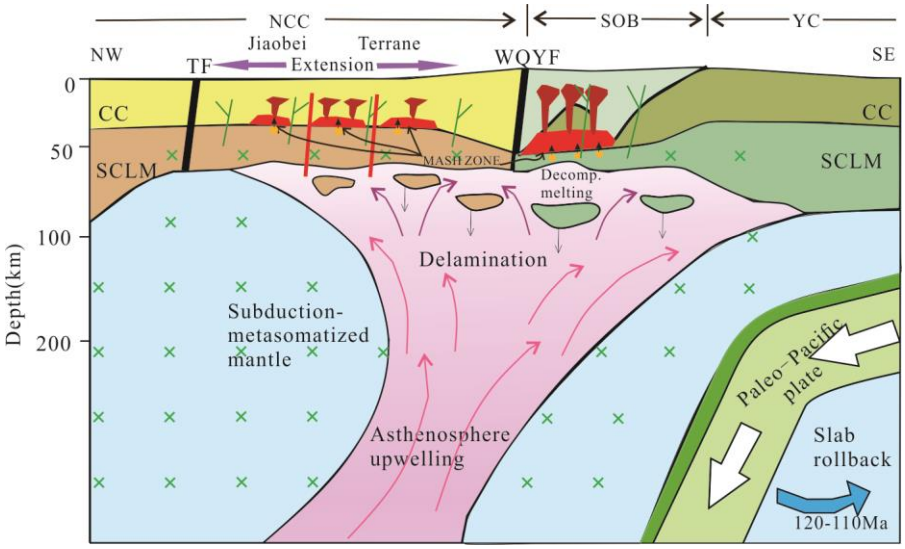


Figure 12. Schematic tectonic model illustrating the generation of the high Ba-Sr Dazeshan granitoids and their dark enclaves (see text for details). Adapted with permission from [33,47,52]. MASH—melting, assimilation, storage, and homogenization; SCLM—subcontinental lithospheric mantle; SOB—Sulu orogenic belt; NCC—North China craton; YC—Yangtze craton; CC—continental crust; WQYF—Wulian-Qingdao-Yantai Fault; TF—Tan-Lu fault.

In summary, on the basis of the petrography, major and trace element geochemistry, geochronology and Sr- and Nd-isotope data of the Dazeshan granitoids and their microgranular dark enclaves, a MASH process followed by the liquid immiscible is envisaged for the origin of late Early Cretaceous granitoids in the Jiaodong Peninsula (Figure 12). It is suggested that at c. 120 Ma, partial melting of ancient continental lower crust in the Jiaodong Peninsula (mainly the Neoarchean-Palaeoproterozoic basement rocks in the Jiaobei terrane) containing a subduction-related material, which resulted from the addition of the enriched subcontinental lithospheric mantle-derived melts, generated the major melts of the Dazeshan granitoids. Then, the mantle-derived basic melts were assimilated by the crust-derived acid melts, forming the homogeneous magma chamber at the crust base (Figure 12). During the homogeneous magma ascent, the single melt split into two immiscible liquids due to the variations in densities, viscosities and temperatures, with one granitic liquid producing Dazeshan granitoids, whereas the other intermediate melt formed the dark enclave (Figure 12).

5.2. Implication for a Shift in Tectonic Setting

Early Cretaceous tectonic evolution history in the Jiaodong Peninsula remains unclear, although it is well documented that its Mesozoic geodynamics are closely associated with the Palaeo-Pacific plate subducting beneath the East China continental margin [11,102,103], and an Early Cretaceous tectonic transition has been identified [8,13]. Large-scale extension-related magmatism [47,52,104] and gold mineralization [6,105], as well as the normal movement along the TLF [9] all suggest an extensional tectonic setting during c. 130–110 Ma in the Jiaodong Peninsula. However, [8] proposed that a tectonic transition from extension to compression occurred in the Jiaodong Peninsula during c. 125–122 Ma, resulting from the shift in subduction direction of the Palaeo-Pacific Plate.

It is widely accepted that the Jiaodong Peninsula has undergone lithospheric thinning during an extensional tectonic setting since the Mesozoic [106–108], which is evidenced by Early Cretaceous high Ba-Sr granitoids in the Jiaobei terrane [33]. However, there is an abrupt change in composition between these two subgroups of Early Cretaceous high Ba-Sr granitoids (Figures 5–9), which indicates a change from juvenile mafic lower crust and continental lower crust sources in the middle Early Cretaceous (132–122 Ma) [33] to continental lower crust and enriched subcontinental lithospheric mantle-derived sources in the late Early Cretaceous (120–110 Ma). Furthermore, the two types of coeval lamprophyres (i.e., low-Ti and high-Ti lamprophyres) emplaced at c. 121 Ma are suggested to originate from an enriched subcontinental lithospheric mantle and an asthenospheric mantle, respectively [47]. It was suggested that the melting of inferred lower crust and juvenile mafic lower crust was caused by asthenosphere upwelling and lithospheric thinning (Figure 13 in [48]), which is in accordance with the Palaeo-Pacific plate WNW-ward subduction, leading to E–W extension in the Jiaodong Peninsula during the middle Early Cretaceous (132–122 Ma) [13,109]. The lithospheric mantle-derived melt for the late Early Cretaceous granitoids (120–110 Ma), combined with the asthenosphere mantle melting for the high-Ti lamprophyres, indicates the Jiaodong Peninsula probably underwent a catastrophic lithospheric thinning event at c. 120 Ma, which is consistent with an abrupt change in the direction of the Palaeo-Pacific plate subducting from WNW to NW at c. 121 Ma [13]. Therefore, this suggests a transition in tectonic setting from E–W extension to NW–SE extension (Figure 12), as also supported by the least principal stress axis shifting from E–W through WNW–ESE to NW–SE c. 119 Ma based on the Palaeostress analysis by the quartz veins and lamprophyre dikes at the Sizhuang gold deposit in the Jiaobei terrane [6].

6. Conclusions

(1) The granitoids of Dazesan pluton consist of medium- to coarse-grained porphyritic-like homogeneous monzogranites, with large amounts of megacrysts of K-feldspar. These rocks possess acid composition, with SiO_2 ranging between 68.25 wt.% and 71.56 wt.% and high K_2O (3.44–5.50 wt.%) and total alkalis (K_2O + Na_2O = 7.29–

9.00 wt.%), with very high Sr (451–638 ppm) and Ba (1157–2842 ppm), showing the typical signatures of high Ba-Sr granitoids.

(2) These granitoids share the same geochemical compositions as those of late Early Cretaceous granitoids. The zircon LA-ICP-MS U-Pb ages of 119.6 ± 1.3 to 120 ± 1 Ma for the granitoids obtained in this study likely represent the lower limit of emplacement ages for the late Early Cretaceous granitoids in the Jiaodong Peninsula.

(3) The microgranular dark enclaves with higher MgO contents of 3.05–4.39 wt.% at lower SiO_2 concentrations of 54.25–56.84 wt.% form a linear trend on the oxide against SiO_2 plots with their host granitoids and have the zircon LA-ICP-MS U-Pb age of 119 ± 2 Ma, identical to those of the host granitoids. Combined with the major-element compositional variation, the relative concentrations of trace and REE elements as well as the similar Sr-Nd isotopic compositions between silicic rocks and their dark enclaves support the liquid immiscibility for their origin.

(4) Partial melting of the ancient continental lower crust in the Jiaodong Peninsula (mainly the Neoarchean-Palaeoproterozoic basement rocks in the Jiaobei terrane) containing a subduction-related material, resulting from the addition of the enriched subcontinental lithospheric mantle-derived melts, generated the crust-derived acid melts, which assimilated the lithospheric mantle-derived basic melts and formed the homogeneous magma chamber at the crust base, then split into two immiscible liquids, with one granitic liquid producing Dazeshan granitoids and the other intermediate one forming the dark enclave during its ascent.

(5) Identification of a lithospheric mantle-derived material in the Dazeshan granitoids suggests a catastrophic lithospheric thinning at c. 120 Ma, in accordance with an abrupt change in direction of Palaeo-Pacific plate subducting, indicating regional tectonic transition from E–W extension to NW–SE extension.

Author Contributions: Conceptualization, Z.W.; Data curation, Z.W.; Formal analysis, R.Z. (Rongxin Zhao), T.Y. and Y.W.; Funding acquisition, Z.W.; Investigation, Z.W., R.Z. (Rongxin Zhao), T.Y., Y.W. and M.W.; Methodology, Z.W.; Project administration, Z.W.; Resources, Z.W. and R.Z. (Rongxin Zhao); Software, X.W., R.Z. (Rifeng Zhang), M.L., Y.L. and J.Q.; Supervision, Z.W.; Validation, Z.W.; Visualization, Z.W.; Writing—original draft, Z.W.; Writing—review and editing, Z.W. All authors have read and agreed to the published version of the manuscript.

Funding: This study was financially supported by the National Key Research and Development Program of China (2022YFC2903602) and the National Natural Science Foundation of China (Grant No. 41772061).

Institutional Review Board Statement: Not applicable.

Informed Consent Statement: Not applicable.

Data Availability Statement: The datasets presented in this study can be obtained upon request to the corresponding author.

Acknowledgments: Constructive comments from the editors, and the revisions from three anonymous reviewers greatly improved the manuscript of this paper. We thank the team members at China University of Geosciences (Beijing) for their field support and comments.

Conflicts of Interest: The authors declare no conflict of interest.

Appendix A

Table A1. Major (wt.%) and trace element (ppm) compositions for dark enclaves and granitoids of the Dazeshan pluton.

Rock Type	Porphyritic-like Monzogranite																Syenodioritic Enclaves				
Sample	DZSD04B1	DZSD04B2-1	DZSD04B2-2	DZSD04B3	DZSD05B1	DZSD06B2-1	DZSD06B2-2	DZSD06B2-3	DZSD06B2-4	DZSD06B2-5	DZSD06B2-6	DZSD14B1-1	DZSD14B1-2	DZSD14B1-3	DZSD14B1-4	DZSD14B1-5	DZSD04B1(bt)	DZSD04B2-1(bt)	DZSD04B2-2(bt)	DZSD05B1(bt)	DZSD06B1(bt)
SiO_2	69.01	69.27	68.65	68.25	70.07	69.54	70.19	70.01	69.15	69	70.25	70.8	71.56	71.44	70.92	68.96	54.33	56.24	56.78	56.84	54.25
TiO_2	0.36	0.327	0.321	0.312	0.275	0.321	0.28	0.318	0.323	0.296	0.329	0.295	0.262	0.326	0.285	0.342	0.993	1.02	0.844	0.698	0.94
Al_2O_3	15.11	15.02	15.33	15.7	15.03	14.82	14.97	14.89	15.25	15.47	14.33	14.31	14.39	13.91	14.49	15.21	17.18	17.63	16.98	16.93	17.96
TFe_2O_3	2.69	2.37	2.33	2.26	2.09	2.47	1.98	2.35	2.4	2.19	2.62	2.35	1.98	2.41	2.19	2.59	8.65	7.09	7.14	6.86	8.02
MnO	0.037	0.033	0.031	0.034	0.029	0.035	0.03	0.037	0.035	0.032	0.036	0.04	0.035	0.04	0.038	0.043	0.145	0.103	0.116	0.127	0.133
MgO	1.11	0.975	0.957	0.94	0.873	1.01	0.83	0.961	0.996	0.882	1.09	1	0.755	0.992	0.924	1.1	4.39	3.36	3.56	3.05	4.24
CaO	2.62	2.4	2.26	2.44	2.28	2.29	2.17	2.5	2.48	2.24	2.79	2.45	2.17	2.37	2.35	2.55	4.52	4.69	4.48	3.81	4.85
Na_2O	3.55	3.51	3.5	3.71	3.64	3.49	3.39	3.8	3.74	3.6	3.85	3.63	3.66	3.5	3.64	3.71	4.67	5.41	4.67	3.82	4.57
K_2O	4.22	4.79	5.5	5.11	4.57	4.43	4.85	3.86	4.26	4.97	3.44	3.88	3.9	3.86	3.96	4.37	3.58	2.64	3.96	6.15	3.12
P_2O_5	0.161	0.136	0.136	0.134	0.125	0.137	0.118	0.133	0.135	0.12	0.152	0.14	0.1	0.14	0.127	0.15	0.482	0.451	0.5	0.671	0.622
LOI	0.58	0.61	0.42	0.54	0.47	0.91	0.65	0.58	0.66	0.64	0.53	0.54	0.62	0.45	0.52	0.43	1.01	1.33	0.92	1.01	0.73
TOTAL	99.448	99.441	99.435	99.43	99.452	99.453	99.458	99.439	99.429	99.44	99.417	99.435	99.432	99.438	99.444	99.455	99.95	99.964	99.95	99.966	99.435
Na_2O/K_2O	0.841	0.733	0.636	0.726	0.796	0.788	0.699	0.984	0.878	0.724	1.119	0.936	0.938	0.907	0.919	0.849	1.304	2.049	1.179	0.621	1.465
Mg#	42.4	42.3	42.3	42.6	42.7	42.2	42.8	42.2	42.5	41.8	42.6	43.1	40.5	42.3	42.9	43.1	47.5	45.8	47.1	44.2	48.5
A/CNK	0.995	0.979	0.968	0.976	0.995	1.007	1.012	0.993	0.997	1.005	0.946	0.977	1.013	0.975	0.995	0.982	0.868	0.868	0.843	0.851	0.910
A/NK	1.450	1.369	1.307	1.348	1.373	1.405	1.381	1.426	1.415	1.367	1.424	1.405	1.403	1.398	1.409	1.402	1.485	1.499	1.417	1.307	1.647
Li	22.6	18.9	20	20.1	19.8	25	20	24.9	21.7	22	21.1	24.3	28.3	22	21.6	26.8	76	59.2	62.7	47.6	72.9
Be	1.43	1.34	1.38	1.27	1.66	1.72	1.56	1.72	2.92	1.56	1.75	1.57	1.66	1.25	1.55	1.55	5.45	5.31	4.72	3.38	4.03
Sc	4.12	3.58	3.66	3.45	3.57	4.87	3.41	3.45	4.66	3.53	4.11	3.88	2.91	3.63	3.81	4.26	21	14.1	16.8	16.2	19.7
V	33.7	31	33.1	29.8	36	37.1	29	30	34.4	28.9	30.1	32.7	21.4	40.7	44.8	34.4	124	102	122	124	106
Cr	17.8	15.6	15.7	14.4	13.3	19.6	13.2	15.2	17.6	15.4	17	14.5	9.88	16	15.1	18.9	133	31.7	22.2	11.9	17
Co	4.98	4.54	4.86	4.34	5.08	5.28	4.03	4.7	4.96	4.19	4.67	4.94	3.59	4.56	4.41	5.78	21.7	16.3	17.3	15.4	20
Ni	7.04	6.05	6.15	6.19	6.08	5.31	5.56	6.2	4.51	5.8	6.75	6.96	4.86	6.19	6.58	5.59	30.4	20.8	13.3	10.1	22.8
Cu	4.96	5.57	9.4	4.4	10.2	0.951	4.39	4.7	0.94	4.27	4.59	4.94	4.21	5.35	4.69	1.18	7.59	9.51	10.4	5.86	23
Zn	29.7	46.6	41.4	39.9	40.3	26.4	25.3	30	28.2	25.7	27	36.3	33.9	31.8	32.9	39.4	117	98.5	101	103	97.6
Ga	18.8	18.9	19.9	18.9	20.2	18.9	18.7	20	19.8	18.5	18.3	20.2	19.1	17.6	17.3	19.4	33.9	31.5	30.1	27.1	34.5
Rb	108	122	137	113	133	127	122	106	123	131	95	108	122	94.4	101	105	202	162	191	216	220
Sr	593	594	638	638	590	602	632	601	632	609	523	555	451	486	564	553	454	535	442	387	544
Nb	7.36	6.97	7.51	7	6.85	9.52	7.44	7.63	9.7	7.18	7.59	7.54	7.58	8.71	7.86	9.04	24	31.4	20.1	15.6	20.9
Mo	0.28	0.955	0.598	0.484	0.577	0.097	0.393	0.368	0.167	0.281	0.284	0.384	0.276	0.353	0.36	0.185	0.347	1.42	1.18	0.289	0.705
Cd	0.051	0.085	0.085	0.058	0.1	0.028	0.067	0.057	0.038	0.056	0.049	0.064	0.08	0.07	0.181	0.018	0.091	0.093	0.079	0.134	0.1
In	0.016	0.021	0.017	0.017	0.017	0.014	0.013	0.013	0.01	0.014	0.014	0.02	0.016	0.022	0.023	0.013	0.065	0.05	0.073	0.074	0.073
Sb	0.027	0.337	0.373	0.326	0.307	0.03	0.04	0.023	0.034	0.025	0.015	0.031	0.017	0.022	0.021	0.041	0.282	0.338	0.236	0.203	0.019
Cs	1.27	1.3	1.61	1.11	1.57	1.9	1.43	1.34	1.57	1.22	1.4	0.959	1.81	0.953	0.879	1.26	7.27	6	5.71	3.76	7.24
Ba	1926	2131	2842	2403	2008	2161	2304	1630	2228	2132	1157	1170	1320	1280	1779	1926	692	629	1135	1413	682
Ta	0.672	0.656	0.709	0.632	0.625	0.725	0.737	0.711	0.802	0.732	0.743	0.692	0.685	0.884	0.723	0.771	1.74	2.95	1.36	1.09	1.4
W	0.091	0.093	0.092	0.13	0.534	0.19	0.11	0.192	0.16	0.22	0.119	0.208	0.246	0.178	0.16	0.136	0.264	0.247	0.227	0.228	0.309
Tl	0.505	0.558	0.678	0.594	0.58	0.638	0.595	0.52	0.598	0.598	0.477	0.505	0.653	0.474	0.462	0.596	1.25	1.01	1.06	1.12	1.08
Pb	18.7	21.2	24.1	24	23.9	21.5	25	22.1	21.5	25.1	18.2	25.7	28.5	21	25.1	26.4	14.4	13.4	16.5	31.6	14.5
Bi	2.03	0.027	0.022	0.021	0.078	0.03	0.024	0.032	0.033	0.043	0.022	0.04	0.03	0.031	0.036	0.054	0.044	0.032	0.04	0.059	0.045
Th	12.6	9.82	14.5	9.51	11	12.7	10.5	10.8	12.9	10.4	15	29	11.2	12.5	11.7	12.8	34.5	20.5	19.1	23.9	22.2
U	1.55	1.62	2.13	1.31	2.13	1.63	1.51	1.31	1.7	1.35	1.45	2.4	1.48	1.23	1.43	2	13.9	8.12	5.43	1.86	3.59
Zr	12.2	11.7	11	8.29	9.51	14.4	12	14	18.4	18	12.5	25.2	26.4	13.3	14.3	13.4	30.3	52.5	48.7	61	60.8
Hf	0.657	0.604	0.607	0.467	0.635	0.879	0.66	0.814	1.1	0.792	0.774	1.02	1.06	0.814	0.793	0.897	1.58	1.83	1.55	1.62	1.89
La	51.6	44.6	46.4	41.1	37.3	57.1	43.7	38.3	45.2	41.1	58	54.4	36.1	47	41.3	47.7	100	70.7	105	154	113
Ce	98.8	89.4	87.9	78.3	72.1	97	71.2	66.1	78.5	73.6	106	91.3	63.2	83.7	69.5	81.5	165	145	179	260	189
Pr	9.22	7.97	8.56	7.19	7.01	9.93	7.67	6.95	8.43	8.17	10.4	9.11	6.41	8.58	7.39	8.59	17.6	20	21.4	29.5	20.8
Nd	30.3	26.7	28	25	22.2	34.9	26.7	25	30.8	26.6	30.3	29.4	21.8	28	26	31.2	57.3	80.1	72.8	92.6	59.6
Sm	4.17	3.92	4.22	3.75	3.39	4.66	3.85	3.67	4.51	4.02	4.36	4.14	3.28	4.19	3.97	4.16	7.6	13.2	9.99	10.6	8.21
Eu	0.965	1.02	1.05	1.13	1.04	0.971	1.1	0.957	0.957	1.21	1.02	1.02	0.776	0.851	0.942	0.984	1.35	2.48	1.74	1.61	1.49
Gd	3.89	3.58	3.83	3.38	2.97	3.51	3.47	3.34	3.29	3.43	4.08	3.85	2.89	3.72	3.41	3.49	7.17	10.3	8.9	11	7.89
Tb	0.52	0.474	0.522	0.413	0.396	0.437	0.463	0.415	0.444	0.475	0.514	0.473	0.377	0.47	0.455	0.484	0.859	1.54	1.1	1.21	1.04
Dy	2.45	2.35	2.44	1.95	1.98	1.96	2.06	1.98	2.1	2.37	2.45	2.27	1.69	2.28	2.06	2.04	3.86	7.08	4.88	5.08	4.82
Ho	0.346	0.317	0.344	0.298	0.285	0.301	0.319	0.314	0.355	0.333	0.326	0.303	0.251	0.337	0.301	0.335	0.622	1.2	0.784	0.734	0.693
Er	1.14	1.02	1.07	0.977	0.823	0.935	0.992	1.05	1.04	1.09	1.08	1.14	0.838	1.14	1.06	1.07	1.83	3.27	2.21	2.39	2.66
Tm	0.137	0.137	0.14	0.121	0.115	0.138	0.136	0.125	0.161	0.136	0.142	0.144	0.11	0.155	0.144	0.146	0.309	0.55	0.373	0.342	0.357
Yb	0.907	0.826	0.877	0.795	0.765	0.823	0.872	0.847	1	0.919	0.869	0.965	0.656	1	0.926	0.927	2.09	3.37	2.4	2.33	2.32
Lu	0.127	0.119	0.127	0.112	0.107	0.122	0.126	0.123	0.134	0.133	0.131	0.148	0.103	0.144	0.138	0.124	0.321	0.469	0.347	0.364	0.356
Y	9.23	8.55	9.11	8.1	7.61	10.2	8.62	8.68	10.9	8.91	9.11	9.2	7.2	9.78	9.1	9.69	19.2	35.6	23.5	22.9	21.7
ΣREE	204.572	182.433	185.48	164.516	150.481	212.787	162.658	149.171	176.921	163.586	219.672	198.663	138.481	181.567	157.596	182.75	365.911	359.259	410.924	571.76	412.236
LREE	195.055	173.61	176.13	156.47	143.04	204.561	154.22	140.977	168.397	154.7	210.08	189.37	131.566	172.321	149.102	174.134	348.85	331.48	389.93	548.31	392.1
HREE	9.517	8.823	9.35	8.046	7.441	8.226	8.438	8.194	8.524	8.886	9.592	9.293	6.915	9.246	8.494	8.616	17.061	27.779	20.994	23.45	20.136
LR/HR	20.495	19.677	18.837	19.447	19.223	24.868	18.277	17.205	19.756	17.409	21.902	20.378	19.026	18.637	17.554	20.211	20.447	11.933	18.573	23.382	19.473
La_N/Yb_N	40.808	38.731	37.951	37.803	34.974	49.766	35.947	32.435	32.422	32.079	47.875	40.436	39.473	33.713	31.992	36.910	34.321	15.048	31.382	47.41	34.937
δEu	0.733	0.832	0.798	0.970	1.002	0.734	0.920	0.836	0.760	0.996	0.739	0.781	0.771	0.659	0.783	0.790	0.559	0.650	0.564	0.456	0.566
Sr/Y	64.247	69.474	70.033	78.765	77.530	59.020	73.318	69.240	57.982	68.350	57.409	60.326	62.639	49.693	61.978	57.069	23.646	15.028	18.809	16.9	25.069
Rb/Sr	0.182	0.205	0.215	0.177	0.225	0.211	0.193	0.176	0.195	0.215	0.182	0.195	0.271	0.194	0.179	0.190	0.445	0.303	0.432	0.558	0.404
Nb/La	0.143	0.156	0.162	0.170	0.184	0.167	0.170	0.199	0.215	0.175	0.131	0.139	0.210	0.185	0.190	0.190	0.240	0.444	0.191	0.101	0.185

References

1. Maruyama, S.; Isozaki, Y.; Kimura, G.; Terabayashi, M. Paleogeographic maps of the Japanese Islands: Plate tectonic synthesis from 750 Ma to the present. *Isl. Arc* **1997**, *6*, 121–142. [CrossRef]
2. Zhu, R.; Chen, L.; Wu, F.; Liu, J. Timing, scale and mechanism of the destruction of the North China Craton. *Sci. China Earth Sci.* **2011**, *54*, 789–797. [CrossRef]
3. Ma, L.; Jiang, S.-Y.; Dai, B.-Z.; Jiang, Y.-H.; Hou, M.-L.; Pu, W.; Xu, B. Multiple sources for the origin of Late Jurassic Linglong adakitic granite in the Shandong Peninsula, eastern China: Zircon U–Pb geochronological, geochemical and Sr–Nd–Hf isotopic evidence. *Lithos* **2013**, *162*, 251–263. [CrossRef]
4. Zhao, Z.; Zheng, Y.-F. Remelting of subducted continental lithosphere: Petrogenesis of Mesozoic magmatic rocks in the Dabie-Sulu orogenic belt. *Sci. China Ser. D Earth Sci.* **2009**, *52*, 1295–1318. [CrossRef]
5. Guo, P.; Santosh, M.; Li, S. Geodynamics of gold metallogeny in the Shandong Province, NE China: An integrated geological, geophysical and geochemical perspective. *Gondwana Res.* **2013**, *24*, 1172–1202. [CrossRef]
6. Wang, Z.; Tranos, M.D.; Wang, X.; Zhao, R.; Zhang, R. ^{40}Ar–^{39}Ar geochronology and palaeostress analysis using lamprophyre dikes and quartz veins in the Sizhuang gold deposit: New implications for Early Cretaceous stress regime in the Jiaodong Peninsula, North China Craton. *Geol. Mag.* **2022**, 1–22. [CrossRef]
7. Xiao, W.; Windley, B.-F.; Hao, J.; Zhai, M. Accretion leading to collision and the Permian Solonker suture, Inner Mongolia, China: Termination of the central Asian orogenic belt. *Tectonics* **2003**, *22*. [CrossRef]
8. Sun, W.; Ding, X.; Hu, Y.-H.; Li, X.-H. The golden transformation of the Cretaceous plate subduction in the west Pacific. *Earth Planet. Sci. Lett.* **2007**, *262*, 533–542. [CrossRef]
9. Zhu, G.; Niu, M.; Xie, C.; Wang, Y. Sinistral to Normal Faulting along the Tan-Lu Fault Zone: Evidence for Geodynamic Switching of the East China Continental Margin. *J. Geol.* **2010**, *118*, 277–293. [CrossRef]
10. Wang, J.; Chang, S.-C.; Lin, P.; Zhu, X.; Fu, Y.; Zhang, H. Evidence of Early Cretaceous transpression in the Sulu orogenic belt, eastern China. *Tectonophysics* **2016**, *687*, 44–55. [CrossRef]
11. Wang, J.; Chang, S.-C.; Chen, Y.; Yan, S. Early Cretaceous transpressional and transtensional tectonics straddling the Sulu orogenic belt, East China. *Geosci. Front.* **2019**, *10*, 2287–2300. [CrossRef]
12. Zhu, G.; Wang, Y.; Liu, G.; Niu, M.; Xie, C.; Li, C. ^{40}Ar/^{39}Ar dating of strike-slip motion on the Tan–Lu fault zone, East China. *J. Struct. Geol.* **2005**, *27*, 1379–1398. [CrossRef]
13. Zhang, B.; Liu, S.; Lin, C.; Shen, W.; Li, X. Reconstruction of the stress regime in the Jiaolai Basin, East Asian margin, as decoded from fault-slip analysis. *J. Struct. Geol.* **2020**, *141*, 104190. [CrossRef]
14. Zhu, R.-X.; Xu, Y.-G. The subduction of the west Pacific plate and the destruction of the North China Craton. *Sci. China Earth Sci.* **2019**, *62*, 1340–1350. [CrossRef]
15. Daoudene, Y.; Ruffet, G.; Cocherie, A.; Ledru, P.; Gapais, D. Timing of exhumation of the Ereendavaa metamorphic core complex (north-eastern Mongolia)—U–Pb and 40Ar/39Ar constraints. *J. Asian Earth Sci.* **2013**, *62*, 98–116. [CrossRef]
16. Tarney, J.; Jones, C.-E. Trace element geochemistry of orogenic igneous rocks and crustal growth models. *J. Geol. Soc.* **1994**, *151*, 855–868. [CrossRef]
17. Qian, Q.; Chung, S.-L.; Lee, T.-Y.; Wen, D.-J. Mesozoic high-Ba-Sr granitoids from North China: Geochemical characteristics and geological implications. *Terra Nova* **2003**, *15*, 272–278. [CrossRef]
18. Choi, S.-G.; Rajesh, V.-J.; Seo, J.; Park, J.-W.; Oh, C.-W.; Pak, S.-J.; Kim, S.-W. Petrology, geochronology and tectonic implications of Mesozoic high Ba-Sr granites in the Haemi area, Hongseong Belt, South Korea. *Isl. Arc* **2008**, *18*, 266–281. [CrossRef]
19. Jiang, N.; Chen, J.; Guo, J.; Chang, G. In situ zircon U–Pb, oxygen and hafnium isotopic compositions of Jurassic granites from the North China craton: Evidence for Triassic subduction of continental crust and subsequent metamorphism-related 18O depletion. *Lithos* **2012**, *142*, 84–94. [CrossRef]
20. Peng, T.; Wilde, S.-A.; Fan, W.; Peng, B. Late Neoarchean potassic high Ba–Sr granites in the Taishan granite–greenstone terrane: Petrogenesis and implications for continental crustal evolution. *Chem. Geol.* **2013**, *344*, 23–41. [CrossRef]
21. Ye, H.-M.; Li, X.-H.; Li, Z.-X.; Zhang, C.-L. Age and origin of high Ba–Sr appinite–granites at the northwestern margin of the Tibet Plateau: Implications for early Paleozoic tectonic evolution of the Western Kunlun orogenic belt. *Gondwana Res.* **2008**, *13*, 126–138. [CrossRef]
22. Ajaji, T.; Weis, D.; Giret, A.; Bouabdellah, M. Coeval potassic and sodic calc-alkaline series in the post-collisional Hercynian Tanncherfi intrusive complex, northeastern Morocco: Geochemical, isotopic and geochronological evidence. *Lithos* **1998**, *45*, 371–393. [CrossRef]
23. Chen, B.; Zhai, M.-G.; Shao, J.-A. Genesis and significance of Mesozoic plutons in northern Taihangshan:geochemical evidence of major and trace elements. *Sci. China, Ser. D.* **2002**, *32*, 896–907, (In Chinese with English abstract). [CrossRef]
24. Fowler, M.; Kocks, H.; Darbyshire, D.; Greenwood, P. Petrogenesis of high Ba–Sr plutons from the Northern Highlands Terrane of the British Caledonian Province. *Lithos* **2008**, *105*, 129–148. [CrossRef]
25. Chen, B.; Jahn, B.-M.; Arakawa, Y.; Zhai, M.-G. Petrogenesis of the Mesozoic intrusive complexes from the southern Taihang Orogen, North China Craton: Elemental and Sr–Nd–Pb isotopic constraints. *Contrib. Miner. Petrol.* **2004**, *148*, 489–501. [CrossRef]

26. Chen, Y.-J.; Pirajno, F.; Qi, J.-P. Origin of Gold Metallogeny and Sources of Ore-Forming Fluids, Jiaodong Province, Eastern China. *Int. Geol. Rev.* **2005**, *47*, 530–549. [CrossRef]
27. Rudnick, R.; Fountain, D.-M. Nature and composition of the continental crust: A lower crustal perspective. *Rev. Geophys.* **1995**, *33*, 267–309. [CrossRef]
28. Guo, F.; Fan, W.; Wang, Y.; Zhang, M. Origin of early Cretaceous calc-alkaline lamprophyres from the Sulu orogen in eastern China: Implications for enrichment processes beneath continental collisional belt. *Lithos* **2004**, *78*, 291–305. [CrossRef]
29. Wu, F.-Y.; Lin, J.-Q.; Wilde, S.; Zhang, X.; Yang, J.-H. Nature and significance of the Early Cretaceous giant igneous event in eastern China. *Earth Planet. Sci. Lett.* **2005**, *233*, 103–119. [CrossRef]
30. Zhang, H.; Zhai, M.; Tong, Y. Petrogenesis of the Sanfoshan High-Ba-Sr Granite, Jiaodong Peninsula, Eastern China. *Geol. Rev.* **2006**, *52*, 43–53. [CrossRef]
31. Wang, Z.-L.; Gong, Q.-J.; Sun, X.; Wu, F.-F.; Wang, W.-X. LA-ICP-MS Zircon U-Pb Geochronology of Quartz Porphyry from the Niutougou Gold Deposit in Songxian County, Henan Province. *Acta Geol. Sin. Engl. Ed.* **2012**, *86*, 370–382. [CrossRef]
32. Faure, M.; Lin, W.; Breton, N.-L. Where is the North China–South China block boundary in eastern China? *Geology* **2001**, *29*, 119–122. [CrossRef]
33. Wang, Z.-L.; Zhao, R.-X.; Zhang, Q.; Lu, H.-W.; Li, J.-L.; Cheng, W. Magma mixing for the high Ba-Sr Guojialing-type granitoids in Northwest Jiaodong Peninsula: Constraints from petrogeochemistry and Sr-Nd isotopes. *Acta Petrol. Sin.* **2014**, *30*, 2595–2608. (In Chinese with English abstract)
34. Zhang, H.-F.; Sun, M.; Zhou, X.-H.; Zhou, M.-F.; Fan, W.-M.; Zheng, J.-P. Secular evolution of the lithosphere beneath the eastern North China Craton: Evidence from Mesozoic basalts and high-Mg andesites. *Geochim. Et Cosmochim. Acta* **2003**, *67*, 4373–4387. [CrossRef]
35. Jahn, B.-M.; Liu, D.; Wan, Y.; Song, B.; Wu, J. Archean crustal evolution of the Jiaodong Peninsula, China, as revealed by zircon SHRIMP geochronology, elemental and Nd-isotope geochemistry. *Am. J. Sci.* **2008**, *308*, 232–269. [CrossRef]
36. Liu, F.; Gerdes, A.; Liu, P. U–Pb, trace element and Lu–Hf properties of unique dissolution–reprecipitation zircon from UHP eclogite in SW Sulu terrane, eastern China. *Gondwana Res.* **2012**, *22*, 169–183. [CrossRef]
37. Zhou, X.-W.; Zhao, G.-C.; Wei, C.-J.; Geng, Y.-S.; Sun, M. EMPA U–Th–Pb monazite and SHRIMP U–Pb zircon geochronology of high-pressure politic granulites in the Jiaobei massif of the North China Craton. *Am. J. Sci.* **2008**, *308*, 328–350. [CrossRef]
38. Tang, J.; Zheng, Y.-F.; Wu, Y.-B.; Gong, B.; Liu, X. Geochronology and geochemistry of metamorphic rocks in the Jiaobei terrane: Constraints on its tectonic affinity in the Sulu orogen. *Precambrian Res.* **2007**, *152*, 48–82. [CrossRef]
39. Faure, M.; Monié, P.; Bruguier, O.; Lin, W. Palaeoproterozoic arc magmatism and collision in Liaodong Peninsula (north-east China). *Terra Nova* **2004**, *16*, 75–80. [CrossRef]
40. Li, S.; Xiao, Y.; Liou, D.; Chen, Y.; Ge, N.; Zhang, Z.; Sun, S.-S.; Cong, B.; Zhang, R.; Hart, S.R.; et al. Collision of the North China and Yangtse Blocks and formation of coesite-bearing eclogites: Timing and processes. *Chem. Geol.* **1993**, *109*, 89–111. [CrossRef]
41. Tang, J.; Zheng, Y.-F.; Wu, Y.-B.; Gong, B.; Zha, X.; Liu, X. Zircon U–Pb age and geochemical constraints on the tectonic affinity of the Jiaodong terrane in the Sulu orogen, China. *Precambrian Res.* **2008**, *161*, 389–418. [CrossRef]
42. Liu, Y.; Wei, J.; Zhang, D.; Chen, J.; Zhang, X. Early Cretaceous Wulong intermediate-mafic dike swarms in the Liaodong Peninsula: Implications for rapid lithospheric delamination of the North China Craton. *Lithos* **2020**, *362–363*, 105473. [CrossRef]
43. Cong, B.L. *Ultrahigh-Pressure Metamorphic Rocks in the Dabieshan–Sulu Region of China*; Science Press: Beijing, China, 1996; p. 224.
44. Zheng, Y.-F. Neoproterozoic magmatic activity and global change. *Sci. Bull.* **2003**, *48*, 1639–1656. [CrossRef]
45. Tang, J.F.; Liu, Y.L.; Wang, Q.F. Geochronology of Mesozoic volcanic rocks in Shandong province. *Acta Petrol. Sin.* **2008**, *24*, 1333–1338.
46. Hacker, B.R. Pressures and Temperatures of Ultrahigh-Pressure Metamorphism: Implications for UHP Tectonics and H_2O in Subducting Slabs. *Int. Geol. Rev.* **2006**, *48*, 1053–1066. [CrossRef]
47. Ma, L.; Jiang, S.-Y.; Hou, M.-L.; Dai, B.-Z.; Jiang, Y.-H.; Yang, T.; Zhao, K.-D.; Pu, W.; Zhu, Z.-Y.; Xu, B. Geochemistry of Early Cretaceous calc-alkaline lamprophyres in the Jiaodong Peninsula: Implication for lithospheric evolution of the eastern North China Craton. *Gondwana Res.* **2014**, *25*, 859–872. [CrossRef]
48. Wang, Z.-L.; Yang, L.-Q.; Deng, J.; Santosh, M.; Zhang, H.-F.; Liu, Y.; Li, R.-H.; Huang, T.; Zheng, X.-L.; Zhao, H. Gold-hosting high Ba-Sr granitoids in the Xincheng gold deposit, Jiaodong Peninsula, East China: Petrogenesis and tectonic setting. *J. Asian Earth Sci.* **2014**, *95*, 274–299. [CrossRef]
49. Hou, M.-L.; Jiang, Y.-H.; Jiang, S.-Y.; Ling, H.-F.; Zhao, K.-D. Contrasting origins of late Mesozoic adakitic granitoids from the northwestern Jiaodong Peninsula, east China: Implications for crustal thickening to delamination. *Geol. Mag.* **2007**, *144*, 619–631. [CrossRef]
50. Zhang, J.; Zhao, Z.-F.; Zheng, Y.-F.; Dai, M. Postcollisional magmatism: Geochemical constraints on the petrogenesis of Mesozoic granitoids in the Sulu orogen, China. *Lithos* **2010**, *119*, 512–536. [CrossRef]
51. Li, L.; Li, S.-R.; Santosh, M.; Li, Q.; Gu, Y.; Lü, W.-J.; Zhang, H.-F.; Shen, J.-F.; Zhao, G.-C. Dyke swarms and their role in the genesis of world-class gold deposits: Insights from the Jiaodong peninsula, China. *J. Southeast Asian Earth Sci.* **2016**, *130*, 2–22. [CrossRef]

52. Ma, L.; Jiang, S.-Y.; Hofmann, A.W.; Xu, Y.-G.; Dai, B.-Z.; Hou, M.-L. Rapid lithospheric thinning of the North China Craton: New evidence from cretaceous mafic dikes in the Jiaodong Peninsula. *Chem. Geol.* **2016**, *432*, 1–15. [CrossRef]
53. Liu, Y.; Hu, Z.; Gao, S.; Günther, D.; Xu, J.; Gao, C.; Chen, H. In situ analysis of major and trace elements of anhydrous minerals by LA-ICP-MS without applying an internal standard. *Chem. Geol.* **2008**, *257*, 34–43. [CrossRef]
54. Andersen, T. Correction of common lead in U–Pb analyses that do not report 204Pb. *Chem. Geol.* **2002**, *192*, 59–79. [CrossRef]
55. Ludwig, K.R. User's Manual for Isoplot 4.16: A Geochronological Toolkit for Microsoft Excel. *Berkeley Geochronol. Cent. Spec.* **2003**, *4*, 25–32.
56. Li, S.; Suo, Y.; Li, X.; Zhou, J.; Santosh, M.; Wang, P.; Wang, G.; Guo, L.; Yu, S.; Lan, H.; et al. Mesozoic tectono-magmatic response in the East Asian ocean-continent connection zone to subduction of the Paleo-Pacific Plate. *Earth Sci. Rev.* **2019**, *192*, 91–137. [CrossRef]
57. Wang, W.; Liu, S.; Bai, X.; Li, Q.; Yang, P.; Zhao, Y.; Zhang, S.; Guo, R. Geochemistry and zircon U–Pb–Hf isotopes of the late Paleoproterozoic Jianping diorite–monzonite–syenite suite of the North China Craton: Implications for petrogenesis and geodynamic setting. *Lithos* **2013**, *162–163*, 175–194. [CrossRef]
58. Pu, W.; Zhao, K.D.; Ling, H.F.; Jiang, S.Y. High precision Nd isotope measurement by Triton TI mass spectrometry. *Acta Geosci. Sin.* **2004**, *25*, 271–274, (In Chinese with English abstract).
59. Pu, W.; Gao, J.F.; Zhao, K.D.; Ling, H.F.; Jiang, S.Y. Separation method of Rb–Sr, Sm–Nd using DCTA and HIBA. Journal of Nanjing University. *Nat. Sci.* **2005**, *41*, 445–450, (In Chinese with English abstract).
60. Hoskin, P.W.O.; Schaltegger, U. The Composition of Zircon and Igneous and Metamorphic Petrogenesis. *Rev. Miner. Geochem.* **2003**, *53*, 27–62. [CrossRef]
61. Middlemost, E.A.K. Naming materials in the magma/igneous rock system. *Earth-Sci. Rev.* **1994**, *37*, 215–224. [CrossRef]
62. Peccerillo, A.; Taylor, S.R. Geochemistry of eocene calc-alkaline volcanic rocks from the Kastamonu area, Northern Turkey. *Contrib. Miner. Petrol.* **1976**, *58*, 63–81. [CrossRef]
63. Maniar, P.D.; Piccoli, P.M. Tectonic discrimination of granitoids. *Geol. Soc. Am. Bull.* **1989**, *101*, 635–643. [CrossRef]
64. Hu, F.F.; Fan, H.R.; Yang, J.H.; Zhai, M.G.; Jin, C.W. Magma mixing for the origin of granodiorite: Geochemical, sr-nd isotopic and zircon hf isotopic evidence of dioritic enclaves and host rocks from changshannan granodiorite in the jiaodong peninsula, eastern china. *Acta Petrol Sin.* **2005**. [CrossRef]
65. Goss, S.C.; Wilde, S.A.; Wu, F.; Yang, J. The age, isotopic signature and significance of the youngest Mesozoic granitoids in the Jiaodong Terrane, Shandong Province, North China Craton. *Lithos* **2010**, *120*, 309–326. [CrossRef]
66. Li, S.; Zhao, G.; Dai, L.; Liu, X.; Zhou, L.; Santosh, M.; Suo, Y. Mesozoic basins in eastern China and their bearing on the deconstruction of the North China Craton. *J. Asian Earth Sci.* **2012**, *47*, 64–79. [CrossRef]
67. Yang, K.-F.; Fan, H.-R.; Santosh, M.; Hu, F.-F.; Wilde, S.A.; Lan, T.-G.; Lu, L.-N.; Liu, Y.-S. Reactivation of the Archean lower crust: Implications for zircon geochronology, elemental and Sr–Nd–Hf isotopic geochemistry of late Mesozoic granitoids from northwestern Jiaodong Terrane, the North China Craton. *Lithos* **2012**, *146*, 112–127. [CrossRef]
68. Zindler, A.; Hart, S.R. Chemical geodynamics. *Annu. Rev. Earth Planet. Sci.* **1986**, *14*, 493–571. [CrossRef]
69. Yang, J.-H.; Chung, S.-L.; Zhai, M.-G.; Zhou, X.-H. Geochemical and Sr–Nd–Pb isotopic compositions of mafic dikes from the Jiaodong Peninsula, China: Evidence for vein-plus-peridotite melting in the lithospheric mantle. *Lithos* **2004**, *73*, 145–160. [CrossRef]
70. Zhang, J.; Zhang, H.-F.; Ying, J.-F.; Tang, Y.-J.; Niu, L.-F. Contribution of subducted Pacific slab to Late Cretaceous mafic magmatism in Qingdao region, China: A petrological record. *Isl. Arc* **2008**, *17*, 231–241. [CrossRef]
71. Yang, J.-H.; Wu, F.-Y.; Wilde, S.A. A review of the geodynamic setting of large-scale Late Mesozoic gold mineralization in the North China Craton: An association with lithospheric thinning. *Ore Geol. Rev.* **2003**, *23*, 125–152. [CrossRef]
72. Gao, S.; Rudnick, R.L.; Yuan, H.L.; Liu, X.M.; Liu, Y.S.; Xu, W.L.; Ling, W.L.; Ayers, J.; Wa-ng, X.C.; Wang, Q.H. Recycling lower continental crust in the North China craton. *Nature* **2004**, *432*, 892–897. [CrossRef] [PubMed]
73. Yang, Q.; Santosh, M.; Shen, J.; Li, S. Juvenile vs. recycled crust in NE China: Zircon U–Pb geochronology, Hf isotope and an integrated model for Mesozoic gold mineralization in the Jiaodong Peninsula. *Gondwana Res.* **2014**, *25*, 1445–1468. [CrossRef]
74. Rudnick, R.; McLennan, S.; Taylor, S. Large ion lithophile elements in rocks from high-pressure granulite facies terrains. *Geochim. Et Cosmochim. Acta* **1985**, *49*, 1645–1655. [CrossRef]
75. Xin, W.; Sun, F.-Y.; Zhang, Y.-T.; Fan, X.-Z.; Wang, Y.-C.; Li, L. Mafic–intermediate igneous rocks in the East Kunlun Orogenic Belt, northwestern China: Petrogenesis and implications for regional geodynamic evolution during the Triassic. *Lithos* **2019**, *346–347*, 346–347. [CrossRef]
76. Fowler, M.B.; Henney, P.J.; Darbyshire, D.P.F.; Greenwood, P.B. Petrogenesis of high Ba–Sr granites: The Rogart pluton, Sutherland. *J. Geol. Soc.* **2001**, *158*, 521–534. [CrossRef]
77. Song, M.C.; Yan, Q.L. Characteristics of Dioritic Inclusions in Weideshan Superunit and Its Magma Origin in Jiaonan Area. *Geol. Shandong* **2000**, *4*, 16–21.
78. Li, X.-C.; Fan, H.-R.; Santosh, M.; Hu, F.-F.; Yang, K.-F.; Lan, T.-G.; Liu, Y.; Yang, Y.-H. An evolving magma chamber within extending lithosphere: An integrated geochemical, isotopic and zircon U–Pb geochronological study of the Gushan granite, eastern North China Craton. *J. Southeast Asian Earth Sci.* **2012**, *50*, 27–43. [CrossRef]

79. Eberz, G.; Nicholls, I.; Maas, R.; McCulloch, M.; Whitford, D. The Nd- and Sr-isotopic composition of I-type microgranitoid enclaves and their host rocks from the Swifts Creek Pluton, southeast Australia. *Chem. Geol.* **1990**, *85*, 119–134. [CrossRef]
80. Bender, J.; Hanson, G.; Bence, A. The Cortlandt complex: Evidence for large-scale liquid immiscibility involving granodiorite and diorite magmas. *Earth Planet. Sci. Lett.* **1982**, *58*, 330–344. [CrossRef]
81. Vernon, R.H. Microgranitoid enclaves in granites—Globules of hybrid magma quenched in a plutonic environment. *Nature* **1984**, *309*, 438–439. [CrossRef]
82. Mezger, K.; Okrusch, M. Metamorphism of the variegated sequence at Kallithea, Samos, Greece. *Miner. Pet.* **1985**, *34*, 67–82. [CrossRef]
83. Holden, P.; Halliday, A.N.; Stephens, W.E. Neodymium and strontium isotope content of microdiorite enclaves points to mantle input to granitoid production. *Nature* **1987**, *330*, 53–56. [CrossRef]
84. Yang, J.H.; Wu, F.Y.; Wilde, S.A.; Liu, X.M. Petrogenesis of late triassic granitoids and their enclaves with implications for post-collisional lithospheric thinning of the liaodong peninsula, north china craton. *Chem. Geol* **2007**, *242*, 155–175. [CrossRef]
85. Lan, T.-G.; Fan, H.-R.; Santosh, M.; Hu, F.-F.; Yang, K.-F.; Yang, Y.-H.; Liu, Y. Early Jurassic high-K calc-alkaline and shoshonitic rocks from the Tongshi intrusive complex, eastern North China Craton: Implication for crust–mantle interaction and post-collisional magmatism. *Lithos* **2012**, *140*, 183–199. [CrossRef]
86. Eichelberger, J.C. Vesiculation of mafic magma during replenishment of silicic magma reservoirs. *Nature* **1980**, *288*, 446–450. [CrossRef]
87. Eby, G.N. Mount Johnson, Quebec-An example of silicate-liquid immiscibility? *Geology* **1979**. [CrossRef]
88. Wiebe, R.A. Fractionation and Liquid Immiscibility in an Anorthositic Pluton of the Nain Complex, Labrador. *J. Pet.* **1979**, *20*, 239–269. [CrossRef]
89. Mezger, K.; Altherr, R.; Okrusch, M.; Henjes-Kunst, F.; Kreuzer, H. Genesis of acid/basic rock associations: A case study The Kallithea intrusive complex, Samos, Greece. *Contrib. Miner. Pet.* **1985**, *90*, 353–366. [CrossRef]
90. Bailey, J.C. Geochemistry and origin of hornblende-bearing xenoliths in the I-type Petford Granite, North-East Queensland. *Aust. J. Earth Sci.* **1984**, *31*, 7–23. [CrossRef]
91. Mcbirney, A.R. Oceanic Volcanism: A Review. *Rev. Geophy.* **1971**, *9*, 523–556. [CrossRef]
92. Rutherford, P.H. Impurity transport in the Pfirsch-Schluter regime. *Phys. Fluids* **1974**, *17*, 1782. [CrossRef]
93. Watson, E.B. Two-liquid partition coefficients: Experimental data and geochemical implications. *Contrib. Miner. Pet.* **1976**, *56*, 119–134. [CrossRef]
94. Ryerson, F.; Hess, P. Implications of liquid-liquid distribution coefficients to mineral-liquid partitioning. *Geochim. Et Cosmochim. Acta* **1978**, *42*, 921–932. [CrossRef]
95. Roedder, E. Silicate Liquid Immiscibility in Magmas. In *The Evolution of the Igneous Rocks, 50th Anniversary Perspectives*; Yoder, H.S., Ed.; Princeton University Press: Princeton, NJ, USA, 1979; p. 588.
96. Philpotts, J.A.; Martin, W.; Schnetzler, C. Geochemical aspects of some Japanese lavas. *Earth Planet. Sci. Lett.* **1971**, *12*, 89–96. [CrossRef]
97. Cawthorn, R.G.; McIver, J.R.; McCarthy, T.S.; Wyatt, B.A.; Ferguson, J.; Barnes, S.J. Possible Liquid Immiscibility Textures in High-Magnesia Basalts from the Ventersdorp Supergroup, South Africa. *J. Geol.* **1979**, *87*, 105–113. [CrossRef]
98. Liu, Y.S.; Gao, S.; Luo, T.C. Geochemistry of Granulites in North China Craton: Implications for The Composition of Archean Lower Crust. *Geol. Geochem.* **1999**, *3*, 40–46.
99. Miller, C.F.; McDowell, S.M.; Mapes, R.W. Hot and cold granites? Implications of zircon saturation tem-peratures and preservation of inheritance. *Geology* **2003**, *31*, 529–532. [CrossRef]
100. Wang, J.; Chang, S.-C.; Lu, H.-B.; Zhang, H.-C. Detrital zircon U–Pb age constraints on Cretaceous sedimentary rocks of Lingshan Island and implications for tectonic evolution of Eastern Shandong, North China. *J. Asian Earth Sci.* **2014**, *96*, 27–45. [CrossRef]
101. Hildreth, W.; Moorbath, S. Crustal contributions to arc magmatism in the Andes of Central Chile. *Contrib. Miner. Pet.* **1988**, *98*, 455–489. [CrossRef]
102. Menzies, M.; Xu, Y.; Zhang, H.; Fan, W. Integration of geology, geophysics and geochemistry: A key to understanding the North China Craton. *Lithos* **2007**, *96*, 1–21. [CrossRef]
103. Goldfarb, R.J.; Santosh, M. The dilemma of the Jiaodong gold deposits: Are they unique? *Geosci. Front.* **2013**, *5*, 139–153. [CrossRef]
104. Zhang, H.-F. Destruction of ancient lower crust through magma underplating beneath Jiaodong Peninsula, North China Craton: U–Pb and Hf isotopic evidence from granulite xenoliths. *Gondwana Res.* **2012**, *21*, 281–292. [CrossRef]
105. Wang, J.; Chang, S.-C.; Wang, K.-L.; Lu, H.-B.; Zhang, H.-C. Geochronology and geochemistry of Early Cretaceous igneous units from the central Sulu orogenic belt: Evidence for crustal delamination during a shift in the regional tectonic regime. *J. Asian Earth Sci.* **2015**, *112*, 49–59. [CrossRef]
106. Gao, S.; Rudnick, R.L.; Carlson, R.W.; McDonough, W.F.; Liu, Y.-S. Re–Os evidence for replacement of ancient mantle lithosphere beneath the North China craton. *Earth Planet. Sci. Lett.* **2002**, *198*, 307–322. [CrossRef]
107. Zhang, H.-F.; Sun, M.; Zhou, X.-H.; Ying, J.-F. Geochemical constraints on the origin of Mesozoic alkaline intrusive complexes from the North China Craton and tectonic implications. *Lithos* **2005**, *81*, 297–317. [CrossRef]

108. Xu, Y.-G. Diachronous lithospheric thinning of the North China Craton and formation of the Daxin'anling–Taihangshan gravity lineament. *Lithos* **2007**, *96*, 281–298. [CrossRef]
109. Seton, M.; Müller, R.; Zahirovic, S.; Gaina, C.; Torsvik, T.; Shephard, G.; Talsma, A.; Gurnis, M.; Turner, M.; Maus, S.; et al. Global continental and ocean basin reconstructions since 200Ma. *Earth-Sci. Rev.* **2012**, *113*, 212–270. [CrossRef]

Disclaimer/Publisher's Note: The statements, opinions and data contained in all publications are solely those of the individual author(s) and contributor(s) and not of MDPI and/or the editor(s). MDPI and/or the editor(s) disclaim responsibility for any injury to people or property resulting from any ideas, methods, instructions or products referred to in the content.